



**HAL**  
open science

# Fault Source Models Show Slip Rates Measured across the Width of the Entire Fault Zone Best Represent the Observed Seismicity of the Pallatanga–Puna Fault, Ecuador

Nicolas Harrichhausen, Laurence Audin, Stéphane Baize, Kendra Johnson, Céline Beauval, Paul Jarrin, Léo Marconato, Frédérique Rolandone, Hervé Jomard, Jean-Mathieu Nocquet, et al.

► **To cite this version:**

Nicolas Harrichhausen, Laurence Audin, Stéphane Baize, Kendra Johnson, Céline Beauval, et al.. Fault Source Models Show Slip Rates Measured across the Width of the Entire Fault Zone Best Represent the Observed Seismicity of the Pallatanga–Puna Fault, Ecuador. *Seismological Research Letters*, 2024, 95 (1), pp.95-112. 10.1785/0220230217 . irsn-04607595

**HAL Id: irsn-04607595**

**<https://irsn.hal.science/irsn-04607595>**

Submitted on 10 Jun 2024

**HAL** is a multi-disciplinary open access archive for the deposit and dissemination of scientific research documents, whether they are published or not. The documents may come from teaching and research institutions in France or abroad, or from public or private research centers.

L'archive ouverte pluridisciplinaire **HAL**, est destinée au dépôt et à la diffusion de documents scientifiques de niveau recherche, publiés ou non, émanant des établissements d'enseignement et de recherche français ou étrangers, des laboratoires publics ou privés.

Copyright


# Fault source models show slip rates measured across the width of the entire fault zone best represent the observed seismicity of the Pallatanga–Puna fault, Ecuador

Nicolas Harrichhausen<sup>\*1</sup> , Laurence Audin<sup>1</sup> , Stéphane Baize<sup>2</sup> , Kendra L Johnson<sup>3</sup> , Céline Beauval<sup>1</sup> , Paul Jarrin<sup>4</sup> , Léo Marconato<sup>1</sup> , Frédérique Rolandone<sup>5</sup> , Hervé Jomard<sup>2</sup> , Jean-Mathieu Nocquet<sup>4</sup> , Alexandra Alvarado<sup>6</sup> , and Patricia A Mothes<sup>6</sup> 

**Cite this article as** Harrichhausen N., L. Audin, S. Baize, K.L. Johnson, C. Beauval, P. Jarrin, L. Marconato, F. Rolandone, H. Jomard, J-M. Nocquet, A. Alvarado, and P. Mothes (2022). Fault source models show slip rates measured across the width of the entire fault zone best represent the observed seismicity of the Pallatanga–Puna fault, Ecuador, *Seismol. Res. Lett.* **XX**, 1–30, doi: [00.0000/0000000000](https://doi.org/10.0000/0000000000).

[Supplemental Material](#)

---

1. Univ. Grenoble Alpes, Univ. Savoie Mont Blanc, CNRS, IRD, Univ. Gustave Eiffel, ISTerre, Grenoble France,  <https://orcid.org/0000-0001-8953-4292> (NH); 2. BERSIN, Institut de Radioprotection et de Sécurité Nucléaire, Fontenay-aux-Roses, France,  <https://orcid.org/0000-0002-7656-1790> (SB); 3. Global Earthquake Model, Pavia, Italy,  <https://orcid.org/0000-0003-1369-5158> (KJ); 4. Univ. Côte d'Azur, CNRS, Observatoire de la Côte d'Azur, IRD, Géoazur, Valbonne, France,  <https://orcid.org/0000-0001-9874-1330> (PJ); 5. Sorbonne Univ., CNRS-INSU, Institut des Sciences de la Terre Paris, Paris, France,  <https://orcid.org/0000-0001-5339-4275> (FR); 6. Instituto Geofísico, Escuela Politécnica Nacional, Quito, Ecuador,  <https://orcid.org/0000-0003-4901-8175> (AA)

\*Corresponding author: [n.harrichhausen@univ-grenoble-alpes.fr](mailto:n.harrichhausen@univ-grenoble-alpes.fr)

© Seismological Society of America

## 1 Abstract

2 We explore how variation of slip rates in fault source models affect computed earthquake rates of the Pallatanga–Puna fault  
3 system in Ecuador. Determining which slip rates best represent fault-zone seismicity is vital for use in Probabilistic Seismic  
4 Hazard Assessment (PSHA). However, given the variable spatial and temporal scales slip rates are measured over, signif-  
5 icantly different rates can be observed along the same fault. The Pallatanga–Puna fault in southern Ecuador exemplifies a  
6 fault where different slip rates have been measured using methods spanning different spatial and temporal scales, and where  
7 historical data and paleoseismic studies provide a record of large earthquakes over a relatively long time span. We use fault  
8 source models to calculate earthquake rates using different slip rates and geometries for the Pallatanga-Puna fault, and com-  
9 pare the computed magnitude frequency distributions (MFDs) to catalogue MFDs from the fault zone. We show slip rates  
10 measured across the entire width of the fault zone, either based on geodesy or long-term geomorphic offsets, produce com-  
11 puted MFDs that compare more favourably with the catalogue data. Moreover, we show the computed MFDs fit the catalogue  
12 data best when they follow a hybrid-characteristic MFD shape. These results support hypotheses that slip rates derived from  
13 a single fault strand of a fault system do not represent seismicity produced by the entire fault zone.

## 14 Introduction

15 Fault-slip rates are key data used in probabilistic seismic hazard assessment (PSHA) models, however, slip rate variability and  
16 uncertainty pose challenges in how they are incorporated in these calculations. In PSHA, seismic source characterization is  
17 the model component that accounts for the earthquake ruptures expected to impact a region of interest. A seismic source  
18 characterization may utilize both distributed seismicity sources (i.e. area sources or smoothed seismicity) and fault sources  
19 (e.g., [Cornell, 1968](#); [Youngs and Coppersmith, 1985](#); [McGuire, 2008](#); [Gerstenberger et al., 2020](#)). Fault sources are used to  
20 indicate higher confidence in the expected earthquake positions and geometries than the area sources, taking advantage of  
21 geological (or other) data that contribute knowledge of the fault zones' geometries and slip rates ([Brune, 1968](#); [Youngs and  
22 Coppersmith, 1985](#)). The earthquake rates in fault source models are then constrained using fault slip rates. There are a variety  
23 of methods used to observe fault system data and each method may encompass different temporal and spatial scales, thus  
24 potentially resulting in inconsistent information ([Styron, 2019](#)). This is the case for fault-slip rates where different methods  
25 of observation, such as geodesy or paleoseismic studies, can result in conflicting rates being measured (e.g., [Papanikolaou  
26 et al., 2005](#); [Oskin et al., 2007](#); [Baize et al., 2020](#)). As these data directly contribute to PSHA assessments in areas where there  
27 are mapped active faults, it is essential to constrain which slip rate measurements produce earthquake rates that are most  
28 representative of the seismic potential of the zone.

29 Different methodologies for measuring slip rates can result in variable observations of the same fault due to the differences  
30 in the time frame over which they are calculated, and the width of the fault zone over which they are measured (Fig. 1). The  
31 use of Global Navigation Satellite System (GNSS) surface velocities to calculate fault slip rates is limited in time to when the  
32 earliest GNSS positions were available for a certain region, typically resulting in 10 – 30 years of observations ([Elliott et al.,  
33 2016](#)), which may not represent the long-term slip rate. Additionally, the width of the fault zone over which GNSS velocities

34 are measuring deformation is constrained by the spacing of GNSS stations, and is often larger (>10 km) than the width  
35 an entire fault zone. Therefore, the slip rates calculated using these widely spaced velocities may also reflect parallel faults  
36 and/or off-fault deformation (e.g., [Zinke et al., 2014](#); [Gold et al., 2015](#)). Conversely, geological and paleoseismic methods  
37 calculate slip rates spanning over 100 to 100,000 year time scales that encompass the entirety of one or several seismic cycles,  
38 however they may be affected by temporal variability in strain rates. Individual discrete fault strands can be assessed with  
39 focused field work such as paleoseismic trenches, or entire fault zones can be studied using the offset of larger geomorphic  
40 or geologic features. An example where the use of multiple methodologies results in different slip rate observations occurs  
41 along the Pallatanga fault in southern Ecuador, which we investigate in this paper (Fig. 1 and Fig. 2). Slip rates have been  
42 measured along this fault using a geodetically constrained elastic block model ( $7.6\pm 0.1$  mm/yr, [Jarrin, 2021](#)), offset of the  
43 Igualata volcanic edifice (2.4–6.1 mm/yr, [Baize et al., 2020](#)), and offset of channels and lava flows along individual fault  
44 segments (2.1–5.6 mm/yr, [Baize et al., 2020](#)). These slip rates consider a variety of time scales and different widths of the  
45 fault zone and all differ in value and uncertainty (Fig. 1).

46 Which slip rate measurements best represent the deformation contributing to the earthquake hazard of a fault zone is not  
47 well understood. For instance, observations of surface deformation during recent surface rupturing strike-slip earthquakes  
48 show a significant portion (up to 50%) of the total slip is observed off of the main structure (e.g., [Rockwell et al., 2002](#); [Dolan  
49 and Haravitch, 2014](#); [Gold et al., 2015](#); [Milliner et al., 2015, 2016](#); [Antoine et al., 2021](#); [Rodriguez Padilla et al., 2022](#)). One  
50 explanation is that slip is constrained to a single structure at depth and distributed at surface, depending on the maturity of  
51 the fault zone (e.g., [Dolan and Haravitch, 2014](#)). If the majority of the slip is along a single structure at depth that distributes  
52 strain onto many faults at the surface, presumably the slip measured on one of these surface faults will underestimate the  
53 moment release during the earthquake (e.g., [Dolan and Haravitch, 2014](#); [Zinke et al., 2014](#)). Instead, the total slip rate across  
54 the entire fault zone, measured using long-term geomorphic or geodetic slip rates, would be the appropriate rate to use in a  
55 fault source model. However, comparisons of seismic moment rates to geodetic moment rates indicate the geodetic moment  
56 rates are greater, suggesting that some deformation is aseismic and does not contribute to earthquake rates (e.g., [Ward, 1998](#);  
57 [Ojo et al., 2021](#)). Therefore, it is important to establish which slip rates best characterize the hazard from a fault system before  
58 using them in a fault source model.

59 The Pallatanga–Puna fault system (PPF) in southern Ecuador is one of the best studied crustal faults in South America  
60 resulting in multiple slip rate observations (Fig. 1), a historic and paleoseismic record of large earthquakes, and consideration  
61 in regional PSHA models (e.g., [Yepes et al., 2016](#); [Beauval et al., 2018](#)). A geodetic block model ([Jarrin, 2021](#)), geologic and  
62 geomorphic mapping ([Winter et al., 1993](#); [Dumont et al., 2005](#); [Baize et al., 2020](#)), and paleoseismic studies ([Baize et al., 2015](#);  
63 [Champenois et al., 2017](#)) have constrained different slip rates along the fault zone. The fault system runs close to large cities  
64 on the Ecuadorian coast (Guayaquil) and in the central Andean Valley (Riobamba and Ambato). Additionally, it is thought  
65 to have hosted the most destructive earthquake recorded in Ecuador, an M 7.6 earthquake in 1797 that destroyed the city of  
66 Riobamba and killed ~ 25, 000 people ([Egred, 2004](#); [Beauval et al., 2010](#)). The well documented historical earthquake record



67 (Beauval et al., 2010) and the paleoseismic earthquake recurrence record (Baize et al., 2015) not only highlight the importance  
68 of this structure with respect to seismic hazard, they provide an opportunity to examine how the measured slip-rates compare  
69 to longer-term large earthquake frequencies.

70 In this paper, we explore the range of possible earthquake rates permitted by the different slip rates observed on the PPF  
71 with the fault source code: Seismic Hazard and Earthquake Rate in Fault Systems (SHERIFS) (Chartier et al., 2017, 2019). We  
72 use SHERIFS to model earthquake rates using slip rates and geometries of multiple segments of the PPF. We then compare  
73 the computed magnitude frequency distributions (MFDs) from SHERIFS to catalogue MFDs from a region surrounding the  
74 fault and paleoseismic records to analyze which slip rates produce MFDs that are most similar to the observed seismicity. We  
75 use SHERIFS because it allows different fault segments to rupture together or as single segments, and it allows for variation  
76 in slip rates for each fault segment, providing a realistic model of a complex fault system. It also allows the user to explore  
77 uncertainty of many variables, such as fault geometry, slip rates, ratios of on fault to background seismicity, and maximum  
78 magnitude (Chartier et al., 2019). Here, we establish ranges of values for these variables based on previous publications on the  
79 PPF and the seismicity catalogue, and then compare models where slip rates, input MFD shapes, and maximum magnitude  
80 ( $M_{\max}$ ) are varied.

## 81 **Pallatanga–Puna fault system (PPF)**

82 The PPF is a ~ 350 km-long zone of active deformation in Central Ecuador striking northeast from southwest of Puna Island  
83 in the Gulf of Guayaquil to the Central Andes northeast of the city of Ambato (Fig. 2). This fault system represents the  
84 southern-most eastern boundary of the Northern Andean Sliver (NAS), a continental sliver moving northeast at a rate of  
85 5.8–9.5 mm/yr with respect to stable South America as a result of oblique subduction of the Nazca Plate (Egbue and Kellogg,  
86 2010; Nocquet et al., 2014; Mora-Páez et al., 2019). Along this southern boundary, the PPF separates the NAS from the Inca,  
87 or Peruvian, sliver, which moves ~5.5 mm/yr southeast with respect to stable South America (Nocquet et al., 2014; Villegas-  
88 Lanza et al., 2016). Strain along the PPF is more localized than the NAS boundary to the north, where several fault branches  
89 and microblocks result in distributed deformation accommodating NAS sliver motion (e.g., Alvarado et al., 2016; Jarrin,  
90 2021), making the PPF ideal for this study. Additionally, several large historical earthquakes causing significant damage,  
91 including the 1961 M 6.3 to 6.8 Pepinales, 1949 M 6.8 Pelileo, 1911 M 6.1 to 6.3 Cajabamba, 1797 M 7.6 Riobamba, and 1698  
92 M 7.2 to 7.3 Ambato earthquakes, have occurred along the northern portion of the PPF (Fig. 3a, b; Beauval et al., 2010).  
93 Paleoseismic trenching indicates large ( $M > 7$ ) earthquakes occur here every ~ 1000 – 3500 years (Location #3, Fig. 2; Baize  
94 et al., 2015). These rich historic and paleoseismic earthquake records highlight the importance for including the PPF as a  
95 fault source in PSHA models for Ecuador (Parra et al., 2016; Beauval et al., 2018), and provides one of the best earthquake  
96 records in South America to compare fault source models with.

97 Oblique right-lateral relative displacement along the PPF is accommodated by a series of northeast-striking strike-slip  
98 fault segments that step northwards (Fig. 2, Winter et al., 1993; Dumont et al., 2005; Alvarado et al., 2016; Baize et al., 2020).  
99 At the southern end of the PPF, the Puna section of the fault system strikes northeastward towards the Andes through the

100 actively northwest–southeast extending Gulf of Guayaquil (Dumont et al., 2005; Witt et al., 2006) and the Guayas River  
101 estuary. High-levels of sedimentation have buried most of the surface trace of the fault in this region, however, right-lateral  
102 strike-slip segments have been mapped on Santa Clara Island and Puna Island (Dumont et al., 2005). On south Puna Island  
103 offset tranverse faults suggest 5–7 mm/yr right-lateral slip for the Upper Pleistocene across a 1 km-wide fault zone (Dumont  
104 et al., 2005).

105 On the Ecuadorian mainland, the Puna fault connects with the Pallatanga fault and traverses north-northwest across the  
106 Cordillera Occidental of the Andes through the Rio Chimbo, Rio Coco and Rio Pangor Valleys to the base of the extinct  
107 Iguatala Volcano north of Riobamba (Fig. 2, Winter et al., 1993; Baize et al., 2015, 2020; Alvarado et al., 2016). Several over-  
108 lapping fault strands have been mapped through these valleys, however, the most convincing evidence of recent slip occurs  
109 along the Rio Pangor Valley in the Rumipamba area (Winter et al., 1993; Baize et al., 2015, 2020). Offset stream channels  
110 along the eastern slope of the valley indicate a Holocene right-lateral slip rate of 2.9–4.6 mm/yr (Winter et al., 1993). A pale-  
111 oseismic trench across a fault segment on this eastern slope indicates 1.2–3.0 mm/yr of primarily right-lateral slip, during  
112 four  $M > 7$  earthquakes with a recurrence interval of 1000 to 3500 years (Baize et al., 2015).

113 North of Riobamba the PPF cross-cuts a volcanic avalanche deposit and Iguatala, offsetting its extinct volcanic edifice  
114 (Fig. 1). Extensive work by Baize et al. (2020) has resulted in multiple slip rates along this portion of the fault (Fig. 2). Offset  
115 of incised valleys in the 66 ka to 32 ka avalanche deposit indicate 1.0–2.0 mm/yr and 1.0–2.7 mm/yr of right-lateral slip across  
116 two parallel fault strands for a total 2.5–4.2 mm/yr. An offset incised gully on Iguatala suggests a similar 2.4–4 mm/yr of slip  
117 across a single fault strand since 60–40 ka. Offset of the Iguatala edifice across a  $\sim 4$  km wide fault zone indicates 2.4–6.6  
118 mm/yr of right lateral slip since 376 ka.

119 Northeast of Iguatala, the PPF steps northward, crosscutting the extinct Huisla volcano before stepping  $\sim 10$  km northward  
120 again to several parallel northeast striking structures including the Pisayambo fault (Fig. 2). A displaced incised creek formed  
121 in Huisla debris avalanche deposits suggests a slip rate range between 0.3 and 4 mm/yr along a single fault strand (Baize et al.,  
122 2020). The large uncertainty in this estimation results from an incision age range from 180 to 15 ka. Further north along the  
123 Pisayambo fault, an offset 12 – 10 ka glacial moraine also suggests a lesser slip-rate of 0.45–1.4 mm/yr (Champenois et al.,  
124 2017). A  $M 5.0$  surface rupturing earthquake in 2010 shows this strand is active, however, nearby offset glacial deposits are  
125 indicative of parallel faults also accommodating Holocene deformation (Champenois et al., 2017).

126 The eastern boundary of the NAS continues northward from the Pisayambo fault towards the Cosanga fault (north of Fig. 2  
127 map extent), however, the location and kinematics of this portion of the fault are less well constrained (Alvarado et al., 2016).  
128 In addition, where the PPF steps northward at the Iguatala and Huisla volcanoes, the north–south trending Latacunga fold  
129 and thrust belt branches northward, partitioning some of the strain between the NAS and stable South America (Tibaldi and  
130 Ferrari, 1992; Lavenu et al., 1995; Fiorini and Tibaldi, 2012; Alvarado et al., 2016; Baize et al., 2020). This is apparent in a  
131 geodetic-based block model of the NAS where  $7.6 \pm 0.1$  mm/yr of right-lateral slip along the PPF decreases to  $4.8 \pm 0.1$  mm/yr  
132 northeast of the intersection with the Latacunga fold and thrust belt (Jarrin, 2021). In addition to the right-lateral slip, the

133 block model also predicts  $2.2 \pm 0.2$  mm/yr of extension along the entire PPF. Active normal faulting is documented in the Gulf  
134 of Guayaquil (Dumont et al., 2005; Witt et al., 2006), but extension has not been observed along the Pallatanga or Pisayambo  
135 faults to the north.

## 136 Model

137 To compute earthquake rates produced by a segmented PPF, we use SHERIFS version 1.3 ([https://github.com/](https://github.com/tomchartier/SHERIFS)  
138 [tomchartier/SHERIFS](https://github.com/tomchartier/SHERIFS)), an open-source Python code to convert slip rates on fault segments to a moment rate bud-  
139 get, which is then spent incrementally following the shape of a prescribed MFD at the scale of the whole fault system  
140 (Chartier et al., 2017, 2019). Each fault segment's magnitude budget is spent with earthquakes randomly selected from a  
141 list of possible ruptures. This list of ruptures consists of all possible earthquakes on prescribed individual fault segments, or  
142 spanning multiple fault segments, with moment magnitudes ( $M$ ) calculated using a rupture area and scaling relation (Wells  
143 and Coppersmith, 1994). Several studies suggest more appropriate scaling relations for the tectonic setting of the PPF (e.g.,  
144 Hanks and Bakun, 2008; Wesnousky, 2008; Stirling et al., 2013), however, proper implementation of these different scaling  
145 relations in SHERIFS is a significant task outside the scope of this project. Possible fault ruptures are determined by setting  
146 a maximum jump distance for a rupture between fault segments, and a  $M_{\max}$  that limits the maximum length of a rupture  
147 based on the magnitude scaling relation. In addition to the magnitude budget of each fault segment, SHERIFS also uses a  
148 prediction of how much of seismicity is background versus on-fault, as a function of magnitude bins to compute earthquake  
149 rates. It is possible for not all of the magnitude budget of certain fault segments to be spent in order to fit the prescribed MFD  
150 shape. When a fault has a remaining moment budget, it is converted into non-mainshock slip (NMS) expressed as a ratio.  
151 The detailed methodology behind SHERIFS is provided by Chartier et al. (2017, 2019).

152 The primary inputs for SHERIFS are fault segment geometries and a list of possible earthquake ruptures, MFD shapes  
153 defined from the seismicity catalogue of the area surrounding the fault zone, a slip rate range for each fault segment, hypothe-  
154 ses of the proportion of earthquakes that are on-fault versus background as a function of magnitude,  $b$ -values describing the  
155 MFD shapes, and a slip rate sample for each fault segment. Each of these inputs defines an equally weighted logic tree  
156 branch in our model, with the first three branches resulting in 12 independent earthquake rate models (Fig. 4a), and the last  
157 three, with a total of 90 end branches, used to explore uncertainty within each of the 12 independent models (Fig. 4b) We also  
158 expand on the 12 independent models by changing  $M_{\max}$  for three of the best fitting models. Each of these logic tree branches  
159 are described in further detail below and our input and data files for the SHERIFS models are included in the Supplemental  
160 Material. Finally, to constrain which slip rates best reproduce the observed earthquake rates, we compare the absolute values  
161 of the modelled earthquake rates to the catalogue MFD in each model.

## 162 Seismicity catalogues

163 We extracted crustal earthquake events ( $< 35$  km depth) from an area within 25 km of two fault models of the PPF from the  
164 Beauval et al. (2013) Ecuador catalogue to derive MFDs for the fault system (Fig. 3). The original data set was constructed

165 by merging eight local and international catalogues, including events between 1587 and 2009, that were homogenized to  
166 moment magnitude based on an empirical relation taken from earthquakes recorded in multiple datasets (Beauval et al.,  
167 2013). In addition, historical earthquakes (Beauval et al., 2010) with locations and magnitudes based on a macroseismic  
168 intensity database (Egred, 2009) are included (Fig. 3). Although there is significant uncertainty associated with the size  
169 and location of these historical earthquakes, their location error is relatively inconsequential as we are computing regional  
170 MFDs for the entire fault system and by including them, we are able to derive a more robust MFD for larger magnitudes.  
171 Constraining the MFD as best as possible for larger magnitudes is essential as we are using SHERIFS to only produce MFDs  
172 for magnitudes greater than M 4.9. The catalogues were declustered by Beauval et al. (2013) using the Reasenber (1985)  
173 algorithm to remove aftershock and foreshock sequences, along with seismic swarms that bias the catalogue to moderate  
174 and smaller magnitude earthquakes. A sensitivity study by Beauval et al. (2013) showed that varying the parameters of  
175 the declustering algorithm for the catalogue had a very minor effect on the resulting Gutenberg-Richter parameters of the  
176 catalogue MFD. The use of a different algorithm declustering algorithm altogether, such as the Gardner and Knopoff (1974)  
177 method, has also been shown to have a very minor impact on the earthquakes rates and subsequent hazard estimates (e.g.,  
178 Beauval et al., 2020). Finally, we assume time independence for the catalogue and that the catalogue is representative of the  
179 long term, but given that in nature seismicity is temporally variable, there is a degree of aleatoric uncertainty involved in  
180 making this assumption.

181 The first catalogue, which we term Set 1, consists of 391 earthquakes with M 3.4 to M 7.6 extracted from the area around  
182 the entire PPF (Set 1, Fig. 3a). The catalogue consists of seven historical earthquakes, including the three largest earthquakes  
183 with  $M > 7$  that are located close to the surface trace of the Pallatanga fault near Riobamba and Ambato. To the south along  
184 the Puna fault, earthquakes are generally smaller (M 3.4 to M 5.2) and there are more events at depths  $> 20$  km. To the north  
185 along the Pisayambo fault there is a seismic nest, or high concentration of moderate magnitude earthquakes that appear  
186 despite declustering (Fig. 3a). These earthquakes, which constitute  $> 35\%$  of the instrumental seismicity in Ecuador (Yepes  
187 et al., 2016), have been hypothesized to result from volcanic processes (Aguilar et al., 1996). However the 2010 M 5.0 right-  
188 lateral surface rupturing earthquake on the Pisayambo fault occurred within the nest and is indicative of a seismogenic fault  
189 zone (Champenois et al., 2017).

190 Due to the potential that some of the seismicity along the Pisayambo fault is volcanic in origin and the large quantity of  
191 moderate magnitude earthquakes at this location, we also consider a catalogue and fault model that does not include these  
192 data (Set 2, Fig. 3b). For this second catalogue, Set 2, we removed the Pisayambo fault segments and surrounding seismicity  
193 reducing the catalogue to 228 events, which still includes the seven historical earthquakes.

194 We calculated Gutenberg-Richter  $b$ -values (Fig. 3c, d) for each of the extracted catalogues using the Weichert (1980) method  
195 in Hazard Modeller's Toolkit of the OpenQuake engine (Pagani et al., 2014). These calculations are based on completeness  
196 tables, which indicates the lowest magnitude per time for which we expect the catalogue to include all events that occurred.  
197 Due to the low number of events, we adapted the completeness table from Beauval et al. (2013) rather than deriving one

198 from the catalogue. This completeness table is valid for the Cordillera region of Ecuador only, while our extracted catalogue  
199 extends along the Puna fault to the southwest away from the Cordillera. Because of this, we do not consider  $M < 4.5$  as  
200 complete in our MFD calculations. We also do not consider earthquakes with  $M > 6.5$  complete before 1860 due to their  
201 large uncertainties in magnitudes and locations in the historical catalogue (Beauval et al., 2013).

202 In Set 2, there are higher relative rates of large earthquakes ( $M \sim 6$ ) because by removing the Pisayambo seismic nest,  
203 we removed a large number of moderate magnitude earthquakes ( $M \sim 4$ ). Therefore, the MFD shape of this catalogue may  
204 be better described by the hybrid-characteristic earthquake model, which has a high rate of earthquakes with a magnitude  
205 characteristic of the fault and a background of lower magnitude earthquakes with rates that decay exponentially with magni-  
206 tude (Youngs and Coppersmith, 1985; Wu et al., 1995), than a Gutenberg-Richter relationship where earthquake rates decay  
207 exponentially across all magnitude bins (Gutenberg and Richter, 1954). Therefore, we run SHERIFS with two alternative  
208 assumptions of the MFD, a Gutenberg-Richter (GR) or hybrid characteristic earthquake (YC) distributions. Both of these  
209 distributions use the  $b$ -values from each catalogue to describe the exponential decay of rates, and the characteristic mag-  
210 nitude in the YC models ranges from  $[M_{\max} - 0.5]$  to  $[M_{\max}]$ , where  $M_{\max}$  is the predefined maximum magnitude of the  
211 system.

212 The two catalogues and two MFD shapes result in two logic tree branches (Fig. 4a). The first branch distinguishes between  
213 the selected fault segments with Set 1: Including Pisayambo and Set 2: Excluding Pisayambo. The second branch is based  
214 on whether a GR or YC distribution is used as an input into SHERIFS. Another branch of the logic tree is also based on the  
215 uncertainty of the  $b$ -values and is defined by the minimum, median, and maximum of the range of the calculated  $b$ -value  
216 from each catalogue (Fig. 4b). This branch is one of the branches used to explore uncertainty within each of the separate  
217 SHERIFS models defined by the branches in Fig. 4a.

## 218 Fault segment geometry and slip rates

219 We combined the mapped surface trace of the PPF system with our own surficial mapping to delineate fault segments for the  
220 two fault models (Set 1 and Set 2, Fig. 3a, b). Fault traces, compiled from Winter et al. (1993); Dumont et al. (2005); Alvarado  
221 (2012); Baize et al. (2015, 2020); Champenois et al. (2017); Costa et al. (2020), were used to initially delineate the main PPF  
222 (Fig. 2). We then constrained the segmentation of the PPF using a hillshaded 4 m-resolution DEM, from SigTierras of the  
223 Ecuadorian Ministry of Agriculture, Quito (<http://ide.sigtierras.gob.ec/geoportal/>). Segment boundaries  
224 were defined where no clear surface trace could be seen in topography or there was a clear step-over in the fault system.  
225 These boundaries produced 18 fault segments that vary in length between  $\sim 34$  and 11 km (Fig. 5).

226 Fault parameters including seismogenic depths, subsurface geometry, rake, and slip rate are assigned to each individual  
227 fault segment, and therefore can be varied through the fault system. For the Pallatanga and Puna segments we use a fault  
228 dip of  $90^\circ$ , and a depth of 18 km to constrain the subsurface geometry. The depth is based on the lower seismogenic depth of  
229 the fault assigned by Beauval et al. (2018), which corroborates our own analyses of instrumental seismicity as a function of  
230 depth. We use a shallower depth of 12 km and a northwestward dip of  $60^\circ$  to constrain the geometry of the Pisayambo fault,

231 based on fault slip inversion using interferometric synthetic aperture radar (Champenois et al., 2017), and our own analyses  
232 of the instrumental catalogue. We assigned a right-lateral slip sense with a rake of  $180^\circ$  to each fault segment based on the  
233 predominance of strike-slip focal mechanisms along the PPF with a nodal plane that is parallel with the fault zone (Vaca  
234 et al., 2019).

235 Fig. 5 shows the slip rate ranges of each PPF segment in the three slip rate models, which correspond to the final logic  
236 tree branch in Fig. 4a. For Model 1, we use slip rates calculated across individual fault segments, such as from paleoseismic  
237 trenches or the individual fault strands that offset the Guano lava flow southwest of Igualata (Baize et al., 2020). The slip  
238 rates in Model 2 are derived from studies that consider long-term geomorphic or geologic offsets across a wider fault zone,  
239 such as the offset Igualata edifice (Fig. 1, 2). Finally, the slip rates in Model 3 are based on the geodetic block model from  
240 Jarrin (2021). We only use the right-lateral component of slip from the block model as we do not model dip slip. Uncertainty  
241 in slip rate is propagated through our models in SHERIFS by sampling slip rates ( $n = 10$ ) uniformly from the defined ranges  
242 in each model (Fig. 4b).

243 SHERIFS produces a list of possible ruptures each segment participates in based on a maximum rupture jumping distance  
244 between each segment, and a maximum rupture length based on a  $M_{\max}$  rupture area. We selected a maximum rupture jump  
245 distance of 5 km, and an  $M_{\max}$  of 7.6 to constrain the possible earthquakes. A maximum jumping distance of 5 km isolates  
246 ruptures on Pisayambo fault segments (Fig. 5) from the rest of the fault system. The rest of the PPF segments that can rupture  
247 together are limited by  $M_{\max}$  of 7.6, which is the largest magnitude observed in the catalogue. This magnitude also equates to  
248 the  $M_{\max}$  we calculate from the instrumental catalogue data using a cumulative seismic moment method (e.g., Makropoulos  
249 and Burton, 1983) in the OpenQuake Hazard Modeller's Toolkit (Pagani et al., 2014). These constraints result in 107 possible  
250 rupture scenarios with a maximum rupture length of 191 km. In our models where the Pisayambo segments are removed,  
251 the total number of ruptures is reduced by 6 to 101. These lists of ruptures are used by SHERIFS to spend the moment budget  
252 for each fault segment, resulting in earthquake rates for the entire system for each of our models.

253 Paleoseismic studies and the uncertainty of the historical magnitudes suggest larger earthquakes ( $M_{\max} = 7.9$ ) along the  
254 PPF (Beauval et al., 2010; Baize et al., 2015), therefore we also explore a greater  $M_{\max}$  value. To do this, we do not restrict  
255  $M_{\max}$  to  $M_{7.6}$  and allow the largest possible rupture (288 km) based on the length of our fault system segments, resulting in  
256 a  $M_{\max} = 7.8$  and 116 possible rupture combinations. Additionally, to better reflect the paleoseismic and historical catalogue,  
257 we increase the seismogenic depth of the Pallatanga fault to 25 km, which is deeper than the proposed seismogenic depth  
258 from Beauval et al. (2018), but allows for  $M_{\max} = 7.9$  with 114 possible rupture combinations. We use these resulting lists of  
259 ruptures in refined SHERIFS models that do not include the Pisayambo fault or a GR MFD shape, to test the effect larger  
260  $M_{\max}$  has on our final results.

## 261 On-fault earthquake probability

262 SHERIFS computes earthquake rates assuming some of the seismicity occurs off of the main fault. The final calculated earth-  
263 quake rates are the sum of both the on-fault earthquakes and the background seismicity, which is determined by SHERIFS



264 using a user defined probability that earthquakes of a certain magnitude occurs on the fault plane instead of as background  
265 seismicity. These probabilities are defined for 0.5 width magnitude bins (Table 1). In our model, we use the three on-fault  
266 seismicity probability hypotheses from [Chartier et al. \(2019\)](#) in lieu of our own because the uncertainty associated with the  
267 hypocenter locations in the [Beauval et al. \(2013\)](#) catalogue and the location of the main fault plane at depth make it difficult to  
268 determine which hypocenters occur directly on the PPF. Because of these uncertainties, the hypotheses we use are arbitrary,  
269 but they cover a large spread of probabilities for M 5.0 to M 6.5 earthquakes while restricting M > 6.5 to mostly being located  
270 on the PPF. We deem this a reasonable assumption because the probable surface rupture length for strike-slip earthquakes  
271 of this magnitude (> 15–20 km, [Wells and Coppersmith, 1994](#); [Wesnousky, 2008](#)) are more likely to be accommodated by the  
272 through-going PPF. Each of these hypotheses define a logic tree branch within each SHERIFS model (Fig. 4b), allowing us  
273 to propagate the uncertainty associated with the different hypotheses through to our results (e.g., [Chartier et al., 2017, 2019,](#)  
274 [2021](#)).

### 275 Non-mainshock slip (NMS)

276 SHERIFS spends the moment-rate budget for each fault segment iteratively until the input target MFD shape is reached,  
277 which can happen before the entire budget of a fault segment is used. This remaining moment budget is defined as the non-  
278 mainshock slip (NMS), and is expressed as a ratio to the slip-rate budget spent on seismogenic slip. This value can represent  
279 geologic processes, such as fault creep, or if it is high (>30–40%), it can indicate the fault source model is not accurately  
280 reproducing the observed seismicity (e.g., [Chartier et al., 2019](#)). In our initial tests of SHERIFS, we observed that NMS ratios  
281 on segments at the end of the fault system were always higher than the rest of the system, due to the lesser number of large  
282 earthquakes these segments could be involved in compared to segments with two neighboring segments that could rupture  
283 together. We consider this an artifact of the model, and therefore we only consider the overall system NMS in comparisons  
284 of our results.

### 285 MFD comparisons

286 We compare cumulative MFDs from each SHERIFS model to the combined instrumental historical catalogue for the fault  
287 system to determine which slip rate and MFD inputs result in a best fit with the observed seismicity. The MFDs computed in  
288 SHERIFS are represented as green density plots and a mean value of each branch in the logic tree. The range in earthquake  
289 rates represents the propagation of uncertainties in slip rates, *b*-values, and on-fault probability of the seismicity through the  
290 logic tree.

291 The instrumental catalogue that we extracted our two catalogues from does not include uncertainties on magnitudes or  
292 locations of earthquakes ([Beauval et al., 2013](#)), while the historical earthquakes have location and magnitude uncertainties  
293 ([Beauval et al., 2010](#)). To reflect these uncertainties, we calculated 95% confidence intervals around the mean earthquake  
294 rates using the method of [Weichert \(1980\)](#), which is based on the number of events in magnitude bin and assumes the  
295 number of earthquake events follow a Poisson distribution about their mean. Additionally, we also used different catalogues

296 with different buffer zones around the fault system, 25 km (used for  $b$ -value calculation) and 5 km, for comparison with  
297 the computed SHERIFS values. We also change background seismicity zone size to reflect the geographical extent of the  
298 catalogues. The smaller buffer zones and background seismicity zones (5 km) reduce earthquake rates and increase their  
299 associated uncertainty at  $M < 6.0$ ; however, comparing to these catalogues does not alter the major results of our study.  
300 Because of this lack of significant change, we only show one comparison between a 5 km SHERIFS model set and buffer  
301 zone catalogue, while the rest of the 5 km buffer zone catalogue comparisons are included in the Supplemental Material  
302 (Fig. S1; Fig. S2b).

303 From their paleoseismic study south of Riobamba on the Rumipamba segment of the fault (Fig. 5), Baize et al. (2015)  
304 suggest this fault segment experiences one  $M > 7.0$  earthquake every 1000 to 3500 years (Fig. 2), which we compare to our  
305 computed cumulative earthquake rates for this fault segment. The computed rates for this segment include all earthquakes  
306 that rupture it, whether or not a fault jump is involved, and are termed ‘participation rates’ from herein (e.g. Chartier et al.,  
307 2019). We plot the participation rates of the Rumipamba segment as a density plot with a mean rate and compare them with  
308 the paleoseismic earthquake rate, which is plotted as a single vertical purple bar corresponding with the rate uncertainty.  
309 We do not plot uncertainty for paleoseismic magnitude because the cumulative rate for  $M > 7$  includes all magnitudes larger  
310 than this value.

## 311 Results

312 Fig. 6 compares the computed cumulative MFDs, observed cumulative MFDs, and NMS percentages for SHERIFS Models  
313 1-3 (individual fault strand, long-term geomorphic, and geodetic slip rates, respectively). These models either include (Set  
314 1) or exclude (Set 2) the Pisayambo fault and surrounding seismicity, have  $M_{\max} = 7.6$ , and use either a Gutenberg-Richter  
315 (GR) or hybrid-characteristic (YC) shape to fit the computed MFDs.

316 Our results show that all instances of Model 1 (individual fault strand slip-rates) compute cumulative earthquake fre-  
317 quencies for  $M > 6.5$  that are lower than the combined catalogue rates by up an order of magnitude. However, the range in  
318 computed rates in Model 1:GR overlap with the catalogue rates for  $M < 6.5$  (Model 1: GR, Fig. 6a). The mean cumulative  
319 earthquake rates in both Set 1 and Set 2 versions of Model 1:YC underestimate rates for all earthquake magnitudes, and all  
320 of the Model 1 results show the largest NMS ratios (27.0% to 38.6%). However, the general shapes of the YC models are more  
321 similar to that of the catalogue MFD.

322 The computed earthquake rates in Model 2 (long-term geomorphic slip rates) show a better fit with the catalogue cumu-  
323 lative MFDs if the Pisayambo fault is removed and they follow a hybrid-characteristic MFD shape (Set 2, YC, Fig. 6). In  
324 Set 1, Model 2:YC underestimates earthquake rates for  $M < 6.5$  (Fig. 6a). Conversely in Set 2, the mean of the computed  
325 earthquake rates overlaps with the range of rates from the combined historic-instrumental catalogue for  $M > 5.25$ , while the  
326 ranges overlap for the lesser magnitudes (Fig. 6b). For Model 2:GR in Sets 1 and 2, the mean earthquake rates for  $M < 6.0$   
327 are overestimated, although their ranges overlap. The YC versions of Model 2 have higher NMS values (23.1%, 20.3%) than  
328 the GR models (16.3%, 16.4%).



329 The models using Model 3 (geodetic slip rates) have higher cumulative earthquake rates than Model 2, but show similar  
330 trends (Fig. 6). The mean rates in Model 3:GR, in both Set 1 and 2, overestimates cumulative rates for  $M < 5.75$ . In Set 1,  
331 Model 3:YC the mean cumulative rates are lower than the catalogue for  $M < 6.5$ , but overlap with the catalogue for higher  
332 magnitudes. Finally in Set 2, the Model 3:YC mean cumulative rates largely overlap with the range in catalogue rates and  
333 have a relatively low NMS value of 17.0% (Model 3:YC, Fig. 6b). Of all the models shown in Fig. 6, Set 2 Model 2:YC and  
334 Model 3:YC fit best with the catalogue data.

335 Fig. 7 shows cumulative participation rates for the Rumipamba segment of the PPF compared to its paleoseismic earth-  
336 quake rate of one  $M > 7$  earthquake per 1000 to 3500 years (Baize et al., 2015). This paleoseismic earthquake rate overlaps  
337 with the mean value of the participation rates of the Rumipamba segment for all Set 1 models (Fig. 7a). However, only  
338 Model 1 overlaps with the paleoseismic earthquake rates in Set 2 (Fig. 7). Model 2: YC, and Model 3: YC from Set 2, which  
339 have the best overall fit when considering the entire fault system (Fig. 6), have cumulative rates for  $M7.0$ , which are greater  
340 and do not overlap with the paleoseismic earthquake rate.

341 As a variation on the best fitting Set 2 YC models, we also computed earthquake rates using  $M_{\max} = 7.8$  (Fig. 8a) and  
342  $M_{\max} = 7.9$ . Both sets of results are similar so we only show the  $M_{\max} = 7.8$  results here ( $M_{\max} = 7.9$  is shown in Fig. S2).  
343 In these models a larger portion of the moment budget is spent by large earthquakes, so we compute greater rates for earth-  
344 quakes with  $M > 7.5$ . These greater large magnitude rates fit the catalogue rates better, but cause lower rates of earthquakes  
345 with  $M < 7.0$ . This results in the mean rates for all models being lower compared to the mean catalogue rates across most mag-  
346 nitude bins. The spread of rates in Model 3, however, overlaps with the range in rates in the catalogue for most magnitudes  
347 and again has the best fit with the observed rates. Model 3 also has the smallest NMS value of 14.3%.

348 In addition to testing a larger  $M_{\max}$ , we also compare these models to observed rates computed from a catalogue extracted  
349 from a 5 km buffer zone around the PPF (Fig. 8b). This much smaller catalogue still includes most of the larger earthquakes  
350 and results in much lower earthquake rates and larger uncertainties for  $M < 7.0$ . Despite this change, Model 1 still underes-  
351 timates earthquake rates across most magnitude bins. Model 2 and Model 3 fit better for  $M < 7.0$  with the mean computed  
352 rate overlapping with the 95% confidence interval of the observed rates across all magnitudes.

353 Finally, we show the participation rates for the Rumipamba segment for the  $M_{\max} = 7.8$  models (Fig. 8b). Similar to the  
354  $M_{\max} = 7.6$  models (Fig. 7), only the mean cumulative participation rate of Model 1 overlaps with the paleoseismic earthquake  
355 rate from Baize et al. (2015). The range of computed participation rates for Model 2 also overlaps with the paleoseismic  
356 earthquake rates, while there is no overlap between the paleoseismic earthquake rates and Model 3.

## 357 Discussion

358 Our initial results show that the computed earthquake rates from Set 2–Model 2: YC and Model 3:YC, irregardless of  $M_{\max}$ ,  
359 have the best fit with the catalogue earthquake rates of the PPF (Fig. 6). This result suggests the following two implications:  
360 First, slower slip rates derived from studies on single fault strands (Model 1) do not provide enough of a moment budget  
361 to reproduce the observed seismicity of the fault system while maintaining the prescribed MFD shapes. Conversely, the

362 faster geodetic and long-term geomorphic slip rates (Model 3 and to some extent Model 2) better reproduce the observed  
363 seismicity and should be weighted more heavily in a fault source model of the PPF. This result also holds when comparing  
364 the computed rates with catalogue rates from within only 5 km of the fault zone. Second, the inclusion (Set 1) or exclusion (Set  
365 2) of Pisayambo seismic nest has a significant impact on the MFD shape derived from the catalogue and used to constrain that  
366 of the fault system; when it is excluded, the combined historic and instrumental catalogue best follows a hybrid-characteristic  
367 earthquake model (e.g., [Youngs and Coppersmith, 1985](#)).

368 The result that the iterations of Model 1 do not reproduce and largely underestimate the observed seismicity supports the  
369 hypotheses that slip rates measured across single surface strands are not representative of the entire fault system (e.g., [Dolan  
370 and Haravitch, 2014](#); [Zinke et al., 2014](#)). This may be especially relevant in regions of higher fault complexity such as fault  
371 bends, because surface strain may be more distributed across many structures at shallow depths compared to a less segmented  
372 and straighter portion of the fault (e.g., [Visage et al., 2023](#)). Measuring a slip rate across a single one of these structures in a  
373 distributed fault zone would miss slip on parallel fault strands (e.g., 2016 Kaikoura earthquake, [Hamling et al., 2017](#); [Williams  
374 et al., 2018](#)), or off-fault deformation (e.g., 2019 Ridgecrest earthquake, [Antoine et al., 2021](#); [Rodriguez Padilla et al., 2022](#)).  
375 Much of the PPF is characterized by left-stepping restraining bends or step-overs north of a latitude of  $-2.5^\circ$ , and this is where  
376 all of the slip rates used in Model 1 were measured (Fig. 2). Thus for the PPF, the faster geodetic or long-term geomorphic  
377 rates used in Models 2 and 3, and measured across the entire fault zone (Fig. 1), better estimate the fault system seismicity.  
378 These slip rates encompass the strain accumulation of the whole system and they probably are more representative of the  
379 slip rate at depth, where the fault system narrows and large earthquakes tend to nucleate (e.g. [Meissner and Strehlau, 1982](#);  
380 [Sibson, 1982](#); [Das and Scholz, 1983](#); [McNulty, 1995](#); [Dolan and Haravitch, 2014](#)). Despite this conclusion, care still must be  
381 taken when using geodetic and long-term geomorphic slip rates due to the limited temporal scale the geodetic rates cover  
382 ( $< 30$  years) or the long time intervals the geomorphic/geologic offsets may cover ( $>> 10$  ka), which can miss temporal slip-  
383 rate variability. Therefore if possible, as many types of slip-rate measurements as possible should be used and compared in  
384 fault source models.

385 The exclusion of the Pisayambo seismic nest (Set 2) changes the shape of the observed MFD of the PPF, impacting which  
386 SHERIFS model produces an MFD that fits best with the catalogue rates. When the abundant moderate magnitude (M 4.0–  
387 5.5) earthquakes in the nest are included in the MFD, the distribution of rates for  $M < 6.0$  resembles a Gutenberg-Richter  
388 distribution (Fig 3). In this case the Set 1, Model 1:GR, the MFD fits well with  $M < 6.0$  earthquakes but underestimates the  
389 large earthquake frequencies (Fig. 6a). As most of the large ( $M > 6.5$ ) earthquakes are located away from the Pisayambo fault  
390 (Fig. 3), this fit with lower magnitudes may suggest that Set 1 Model 1:GR may work best in computing seismicity for only the  
391 Pisayambo segments. If this seismicity nest is a phenomenon that occurs along the entire PPF, then it would be important to  
392 use it in the analysis of the whole system. However, as the nest has been attributed to local volcanic processes ([Aguilar et al.,  
393 1996](#)), the computed MFD for the entire PPF should not be compared to the seismic nest. Instead, we advise the Pisayambo  
394 fault segments be modeled separately from the rest of the PPF using different inputs derived from a MFD of the seismic nest.

395 In addition to changing the shape of the catalogue MFD (Fig. 3), removing the Pisayambo fault and related seismicity  
396 removes a section of the fault system where we expect there is more distributed deformation. The low slip rate (0.45–1.4  
397 mm/yr) along the Pisayambo fault, may be indicative that strain is being accommodated on parallel fault strands. To the  
398 northeast of the Huisla volcano, several fault strands may branch away from the main structure resembling a horsetail typ-  
399 ical of the end of a fault system (Fig. 2). Also at this location, the Latacunga fold and thrust belt to the east is known to  
400 be accommodating horizontal shortening (Fig. 2, [Tibaldi and Ferrari, 1992](#); [Lavenu et al., 1995](#); [Fiorini and Tibaldi, 2012](#);  
401 [Alvarado et al., 2016](#); [Baize et al., 2020](#)), and active strike-slip faults have been mapped both east and west of the Pisayambo  
402 fault ([Champenois et al., 2017](#)). Therefore, the slip rate measured across only the Pisayambo fault would not represent all of  
403 the seismicity surrounding this structure.

404 The use of different magnitude scaling relations could also change the MFDs produced by SHERIFS. For example, the  
405 length-based scaling relationships of [Wesnousky \(2008\)](#) for strike-slip faults intersects the one for [Wells and Coppersmith](#)  
406 [\(1994\)](#) at ~100 km length, where both predict  $M \sim 7.3$ . For shorter ruptures, [Wesnousky \(2008\)](#) predicts larger magnitudes  
407 than [Wells and Coppersmith \(1994\)](#), and vice versa for rupture lengths  $\geq 100$  km (in the model we use area-based magnitude  
408 scaling relations, but compare two length-based relationships here for consistency). Thus, using [Wesnousky \(2008\)](#) would  
409 mean that the longest ruptures would produce lower magnitude earthquakes than [Wells and Coppersmith \(1994\)](#), reducing  
410 the value of  $M_{\max}$ , and each using less of the seismic moment budget. Since the  $b$ -value is controlled by the modeller, the  
411 impact is likely to be of the same type as changing  $M_{\max}$ , which we discuss below. Finally, as changing  $M_{\max}$  does not alter  
412 our main results concerning slip rate variation (Fig. 8), we interpret that using a different scaling relation would also not  
413 change this outcome.

#### 414 NMS values

415 In addition to producing MFDs that fit better with the catalogue earthquake rates, the faster slip rate models (Models 2 and  
416 3), also result in relatively lower system-wide NMS ratios. These lower NMS ratios are likely the result of the moment budget  
417 allowing for more larger events, thereby increasing the rates of all earthquakes and using more of the moment budget without  
418 violating the shape of the MFD. There are geological processes that could account for NMS such as fault creep. High NMS  
419 percentages  $> 30$ – $40\%$  could also result from the fault-source model not accurately representing the observed seismicity, or  
420 conversely, that a large portion of the observed seismicity is not being produced by the fault (e.g., [Chartier et al., 2019](#)). We  
421 interpret that the higher NMS percentages in Model 1 compared to Models 2 and 3 result from one or a few large earthquakes  
422 spending the entire moment-rate budget of a fault segment, and not allowing other, faster deforming neighboring segments  
423 to be involved in multi-segment ruptures that utilize their remaining moment budgets. This interpretation suggests again  
424 that the moment budget resulting from the lower, Model 1 slip rates, cannot account for all of the fault system seismicity.

425 The models using a Gutenberg-Richter (GR) MFD shape have lower NMS percentages than their hybrid-characteristic  
426 (YC) counterparts (Fig. 6). This result is most likely due to the GR models allowing a larger proportion of moderate sized  
427 earthquakes to spend the slip-rate in smaller increments, permitting the more frequent use of individual segment ruptures.

428 However, because the moment budget is spent on a higher frequency of moderate earthquakes, SHERIFS underestimates  
429 the larger earthquake frequencies resulting in a poorer fit of the GR models with the catalogues compared to the YC models  
430 (Fig. 6).

### 431 Paleoseismic earthquake rates

432 Paleoseismic earthquake rates on the Rumipamba segment (Baize et al., 2015) are lower than the computed participation  
433 rates of the best fitting SHERIFS models (Set 2; Model 2:YC and Model 3:YC), while overlapping with all iterations of Model  
434 1 and all models in Set 1 (Fig. 7). Despite this misfit, we still prefer Set 2; Model 2:YC and Model 3:YC. The reason for  
435 this preference is the paleoseismic earthquake rate for  $M \geq 7$  is also lower than the observed catalogue rate and it may not  
436 accurately record all of the large earthquakes that ruptured the Rumipamba segment of the PPF. The historical catalogue  
437 places, albeit with significant uncertainty, the 1698 M 7.25 and 1645 M 7.0 epicenters along the Rumipamba segment, while  
438 the 1797 M 7.6 earthquake is located  $< 30$  km along-strike to the north (Fig. 3, Beauval et al., 2010). Given their epicenters and  
439 magnitudes, these three earthquakes would have likely ruptured the Rumipamba or parallel fault segments resulting in an  
440 earthquake rate of three  $M \geq 7$  earthquakes in the last 500 years, significantly greater than the paleoseismic earthquake rate  
441 of one  $M \geq 7$  earthquake every 1000 to 3500 years (Baize et al., 2015). This discrepancy demonstrates that, if these historical  
442 earthquakes ruptured the PPF system, the paleoseismic trench does not record every earthquake along this portion of the  
443 PPF.

444 Missing earthquake events in a paleoseismic study are expected and could result from rupture propagation along a par-  
445 allel fault segment, no surface rupture occurring, and/or low sedimentation rates. For example, paleoearthquake detection  
446 probability curves from the Uniform California Earthquake Forearc (UCERF) 3 model (Weldon and Biasi, 2013) and the  
447 2022 New Zealand National Seismic Hazard Model (Coffey et al., 2022) indicate, even at the greatest rupture lengths, a prob-  
448 ability of  $\sim 0.8$  and  $\sim 0.45$  (respectively) that a M 7 earthquake would be detectable in a paleoseismic study. Additionally,  
449 paleoseismic trenching along the El Salvador fault zone, which was recently ruptured by a 2001 M 6.6 earthquake, shows  
450 that earthquakes of this magnitude and lower are difficult to observe in the stratigraphic record (Canora et al., 2012). The  
451 authors of this study suggest that the earthquake recurrence interval from the paleoseismic record of this strike-slip forearc  
452 fault, similar in tectonic setting to the PPF, should be treated as a minimum. These observations further argue that slip rates  
453 and earthquake recurrence intervals observed in paleoseismic studies on a single fault-segment should not be the sole input  
454 into fault source models.

### 455 Impact of $M_{\max}$

456 Using  $M_{\max}$  of 7.8 or 7.9 in the Set 2, YC models results in a better fit of the computed rates with the catalogue rates for  $M > 7.0$ ,  
457 and in the case of the long-term geomorphic model (Model 2), a better fit with the paleo-earthquake data (Fig. 8; Fig. S2).  
458 However, because high magnitude earthquakes utilize a large portion of the moment budget and leave less to be distributed  
459 among lower magnitudes, these models underestimate lower earthquakes rates. Therefore, we interpret these results are not

460 necessarily indicative of the correct  $M_{\max}$  to use for the PPF, and several  $M_{\max}$  values should be input as different branches  
461 of a logic tree in a PSHA model.

462 Although the computed  $M_{\max} = 7.8$  and  $7.9$  MFDs suggest there is not enough moment budget to produce the largest  
463 earthquakes at the observed rates while maintaining the prescribed MFD shape, there are geologic scenarios that can explain  
464 this misfit. For example, we only use strike-slip rates as inputs on the PPF and assume all of the earthquakes are derived from  
465 this slip component. However, at the northern end of the PPF the Latacunga fold and thrust belt branches northward from  
466 the PPF system (Fig. 2; [Tibaldi and Ferrari, 1992](#); [Lavenu et al., 1995](#); [Fiorini and Tibaldi, 2012](#); [Alvarado et al., 2016](#); [Baize  
467 et al., 2020](#)) and probably accommodates some of the convergence modeled by geodesy ([Marinière et al., 2020](#); [Jarrin, 2021](#)).  
468 Some of the observed seismicity (Fig. 3) could result from these structures, or other unmapped reverse faults, and therefore  
469 would not be modelled by our strike-slip rate derived moment budget alone. For example, the 1868 M 7.2 to 7.3 Ambato  
470 earthquake could have occurred on a thrust fault splaying to the north away from the PPF. The same argument holds true  
471 for the southern end of the PPF, where extension in the Gulf of Guayaquil also results in seismicity on normal faults and  
472 resolvable divergence in the geodetic block model (Fig.5; [Witt et al., 2006](#); [Dumont et al., 2005](#); [Jarrin, 2021](#)). Unfortunately  
473 the locations, geometries, and slip rates on the individual dip-slip structures are not well constrained, but further studies of  
474 these structures and incorporating them into our models may improve the fit with the observed seismicity.

## 475 **Conclusions**

476 By using SHERIFS to calculate earthquake rates using different slip rates for the PPF, we find that slip rates measured across  
477 the entire width of the fault zone, such as those based on geodesy or long-term geomorphic offsets, produce MFDs that com-  
478 pare more favourably with the observed catalogue. This result cautions against using only slip rates measured across single  
479 discrete fault segments within a fault zone because these often slower slip rates do not provide enough of a moment budget  
480 to account for fault zone seismicity. This conclusion also suggests that off-fault damage and slip on parallel fault segments  
481 are important to consider in fault source models. We also show the MFDs computed using a YC (hybrid characteristic) MFD  
482 shape, have a better fit with the the observed catalogue when the Pisayambo fault and associated seismic nest are removed (Set  
483 2). Additionally, the model results that best fit the observed catalogue are not consistent with paleoseismic earthquake rates  
484 observed on the Rumipamba section of the PPF. However, as the paleoseismic record suggests that not all of the  $M \geq 7.0$  rup-  
485 tures along the Rumipamba are recorded at the paleoseismic study location, we conclude that this comparison is not robust.  
486 By increasing  $M_{\max}$  in our best fitting models from M 7.6 to M 7.8 or M 7.9, we compute MFDs that slightly underestimate  
487 earthquake rates for all but the largest magnitude bins. However, the additional slip-rate budget required for the increased  
488 moment release could be acquired from dip-slip rates on fault systems that connect with the PPF, which are unaccounted  
489 for in our models. Because of this possibility, using greater  $M_{\max}$  values should be considered as a logic tree branch of a fault  
490 source model of the PPF.

## 491 **Data and Resources**

492 The earthquake catalogues, and SHERIFS data and input files are available in the Supplemental Material. SHERIFS ver-  
493 sion 1.3, along with instruction manuals and examples can be downloaded at: [https://github.com/tomchartier/  
494 SHERIFS](https://github.com/tomchartier/SHERIFS), last accessed 10/01/2023. The OpenQuake Engine 3.15.0, used to analyze the earthquake catalogues is avail-  
495 able at: <https://github.com/gem/oq-engine/releases>, last accessed 09/02/2023. QGIS 3.22.0, used for fault  
496 trace mapping is available at: <https://download.qgis.org/downloads/>, last accessed 23/10/2021. The Copernicus  
497 30 m DEM used in Fig. 2 and Fig. 3 is available at: [https://spacedata.copernicus.eu/collections/  
498 copernicus-digital-elevation-model](https://spacedata.copernicus.eu/collections/copernicus-digital-elevation-model), last accessed 17/09/2021.

## 499 **Competing interests**

500 The authors acknowledge there are no conflicts of interest recorded.

## 501 **Acknowledgements**

502 Funding was provided through a Centre Nationale d'Études Spatiale (CNES) postdoctoral fellowship to N. Harrichhausen  
503 and Institut de Recherche pour le Développement (IRD) grant to L. Audin. The authors would like to thank T. Chartier, O.  
504 Scotti, and S. El Kadri for their thoughtful discussions on using SHERIFS for fault source modelling. Finally, the thoughtful  
505 reviews and comments from two anonymous reviewers and editors A. Bent and K. Berryman were of great help and well  
506 appreciated.

## 507 **References**

- 508 Aguilar, J., J.-L. Chatelain, B. Guillier, and H. Yepes (1996). The Pisayambo, Ecuador, seismicity nest: towards the birth of a volcano? In  
509 *Geodinámica Andina, Troisième symposium international sur la Géodynamique Andine, Collection Colloques et Séminaires*, pp. 126–129.  
510 ORSTOM édition Paris.
- 511 Alvarado, A., L. Audin, J.-M. Nocquet, E. Jaillard, P. Mothes, P. Jarrín, M. Segovia, F. Rolandone, and D. Cisneros (2016). Partitioning of  
512 oblique convergence in the Northern Andes subduction zone: Migration history and the present-day boundary of the North Andean  
513 Sliver in Ecuador. *Tectonics* **35**(5), 1048–1065.
- 514 Alvarado, A. A. C. (2012). *Néotectonique et cinématique de la déformation continentale en Equateur*. Ph. D. thesis, Université de Grenoble.
- 515 Antoine, S. L., Y. Klinger, A. Delorme, K. Wang, R. Bürgmann, and R. D. Gold (2021). Diffuse deformation and surface faulting distribution  
516 from submetric image correlation along the 2019 Ridgecrest, California, ruptures. *Bulletin of the Seismological Society of America* **111**(5),  
517 2275–2302.
- 518 Baize, S., L. Audin, A. Alvarado, H. Jomard, M. Bablon, J. Champenois, P. Espin, P. Samaniego, X. Quidelleur, and J.-L. Le Pennec (2020).  
519 Active tectonics and earthquake geology along the Pallatanga fault, central Andes of Ecuador. *Frontiers in Earth Science* **8**, 193.
- 520 Baize, S., L. Audin, T. Winter, A. Alvarado, L. P. Moreno, M. Taipei, P. Reyes, P. Kauffmann, and H. Yepes (2015). Paleoseismology and  
521 tectonic geomorphology of the Pallatanga fault (Central Ecuador), a major structure of the South-American crust. *Geomorphology* **237**,  
522 14–28.

- 523 Beauval, C., P.-Y. Bard, and L. Danciu (2020). The influence of source-and ground-motion model choices on probabilistic seismic hazard  
524 levels at 6 sites in France. *Bulletin of Earthquake Engineering* **18**, 4551–4580.
- 525 Beauval, C., J. Marinière, H. Yepes, L. Audin, J.-M. Nocquet, A. Alvarado, S. Baize, J. Aguilar, J.-C. Singaicho, and H. Jomard (2018). A  
526 new seismic hazard model for Ecuador. *Bulletin of the Seismological Society of America* **108**(3A), 1443–1464.
- 527 Beauval, C., H. Yepes, W. H. Bakun, J. Egred, A. Alvarado, and J.-C. Singaicho (2010). Locations and magnitudes of historical earthquakes  
528 in the Sierra of Ecuador (1587–1996). *Geophysical Journal International* **181**(3), 1613–1633.
- 529 Beauval, C., H. Yepes, P. Palacios, M. Segovia, A. Alvarado, Y. Font, J. Aguilar, L. Troncoso, and S. Vaca (2013). An earthquake catalog for  
530 seismic hazard assessment in Ecuador. *Bulletin of the Seismological Society of America* **103**(2A), 773–786.
- 531 Brune, J. N. (1968). Seismic moment, seismicity, and rate of slip along major fault zones. *Journal of Geophysical Research* **73**(2), 777–784.
- 532 Canora, C., P. Villamor, J. Martínez-Díaz, K. R. Berryman, J. A. ÁLVAREZ-GÓMEZ, R. Capote, and W. Hernández (2012). Paleoseismic  
533 analysis of the San Vicente segment of the El Salvador Fault Zone, El Salvador, Central America. *Geologica Acta: an international earth  
534 science journal* **10**(2), 103–123.
- 535 Champenois, J., S. Baize, M. Vallée, H. Jomard, A. Alvarado, P. Espin, G. Ekström, and L. Audin (2017). Evidences of surface rupture associ-  
536 ated with a low-magnitude ( $M_w$  5.0) shallow earthquake in the Ecuadorian Andes. *Journal of Geophysical Research: Solid Earth* **122**(10),  
537 8446–8458.
- 538 Chartier, T., O. Scotti, and H. Lyon-Caen (2019). SHERIFS: Open-source code for computing earthquake rates in fault systems and  
539 constructing hazard models. *Seismological Research Letters* **90**(4), 1678–1688.
- 540 Chartier, T., O. Scotti, H. Lyon-Caen, and A. Boiselet (2017). Methodology for earthquake rupture rate estimates of fault networks: example  
541 for the western Corinth rift, Greece. *Natural Hazards and Earth System Sciences* **17**(10), 1857–1869.
- 542 Chartier, T., O. Scotti, H. Lyon-Caen, K. Richard-Dinger, J. H. Dieterich, and B. E. Shaw (2021). Modelling earthquake rates and associated  
543 uncertainties in the Marmara Region, Turkey. *Natural Hazards and Earth System Sciences* **21**(8), 2733–2751.
- 544 Coffey, G., C. Rollins, R. Van Dissen, D. Rhoades, K. Thingbaijam, K. Clark, M. Gerstenberger, N. Litchfield, and A. Nicol (2022). New  
545 zealand national seismic hazard model 2022: earthquake recurrence derivation from paleoseismic data and probability of detection.  
546 *GNS Science report* **2022/32**, 57.
- 547 Cornell, C. A. (1968). Engineering seismic risk analysis. *Bulletin of the Seismological Society of America* **58**(5), 1583–1606.
- 548 Costa, C., A. Alvarado, F. Audemard, L. Audin, C. Benavente, F. H. Bezerra, J. Cembrano, G. González, M. López, E. Minaya, et al. (2020).  
549 Hazardous faults of South America; compilation and overview. *Journal of South American Earth Sciences* **104**, 102837.
- 550 Das, S. and C. Scholz (1983). Why large earthquakes do not nucleate at shallow depths. *Nature* **305**(5935), 621–623.
- 551 Dolan, J. F. and B. D. Haravitch (2014). How well do surface slip measurements track slip at depth in large strike-slip earthquakes? the  
552 importance of fault structural maturity in controlling on-fault slip versus off-fault surface deformation. *Earth and Planetary Science  
553 Letters* **388**, 38–47.
- 554 Dumont, J. F., E. Santana, and W. Vilema (2005). Morphologic evidence of active motion of the Zambapala Fault, Gulf of Guayaquil  
555 (Ecuador). *Geomorphology* **65**(3-4), 223–239.
- 556 Dumont, J.-F., E. Santana, W. Vilema, K. Pedoja, M. Ordonez, M. Cruz, N. Jimenez, and I. Zambrano (2005). Morphological and  
557 microtectonic analysis of quaternary deformation from Puná and Santa Clara islands, Gulf of Guayaquil, Ecuador (South America).  
558 *Tectonophysics* **399**(1-4), 331–350.



- 559 Egbue, O. and J. Kellogg (2010). Pleistocene to present North Andean “escape”. *Tectonophysics* **489**(1-4), 248–257.
- 560 Egred, J. (2004). *Terremoto de Riobamba del 4 Febrero de 1797*, pp. 67–86. Corporación Editora Nacional.
- 561 Egred, J. (2009). Catalogo de terremotos del Ecuador 1541–2009.
- 562 Elliott, J., R. Walters, and T. Wright (2016). The role of space-based observation in understanding and responding to active tectonics and  
563 earthquakes. *Nature communications* **7**(1), 13844.
- 564 Fiorini, E. and A. Tibaldi (2012). Quaternary tectonics in the central Interandean Valley, Ecuador: Fault-propagation folds, transfer faults  
565 and the Cotopaxi Volcano. *Global and Planetary Change* **90**, 87–103.
- 566 Gardner, J. and L. Knopoff (1974). Is the sequence of earthquakes in Southern California, with aftershocks removed, Poissonian? *Bulletin*  
567 *of the seismological society of America* **64**(5), 1363–1367.
- 568 Gerstenberger, M. C., W. Marzocchi, T. Allen, M. Pagani, J. Adams, L. Danciu, E. H. Field, H. Fujiwara, N. Luco, K.-F. Ma, et al. (2020).  
569 Probabilistic seismic hazard analysis at regional and national scales: State of the art and future challenges. *Reviews of Geophysics* **58**(2),  
570 e2019RG000653.
- 571 Gold, R. D., N. G. Reitman, R. W. Briggs, W. D. Barnhart, G. P. Hayes, and E. Wilson (2015). On-and off-fault deformation associated with  
572 the September 2013 Mw 7.7 Balochistan earthquake: Implications for geologic slip rate measurements. *Tectonophysics* **660**, 65–78.
- 573 Gutenberg, B. and C. Richter (1954). *Seismicity of the Earth and Associated Phenomena*. Princeton University Press.
- 574 Hamling, I. J., S. Hreinsdóttir, K. Clark, J. Elliott, C. Liang, E. Fielding, N. Litchfield, P. Villamor, L. Wallace, T. J. Wright, et al. (2017).  
575 Complex multifault rupture during the 2016 M w 7.8 Kaikōura earthquake, New Zealand. *Science* **356**(6334), eaam7194.
- 576 Hanks, T. C. and W. H. Bakun (2008, 02). M-logA Observations for Recent Large Earthquakes. *Bulletin of the Seismological Society of*  
577 *America* **98**(1), 490–494.
- 578 Jarrin, P. (2021). *Cinématique actuelle dans les Andes du Nord par GPS*. Ph. D. thesis, Sorbonne Université.
- 579 Jarrin, P., J.-M. Nocquet, F. Rolandone, H. Mora-Páez, P. Mothes, and D. Cisneros (2023). Current motion and deformation of the Nazca  
580 Plate: new constraints from GPS measurements. *Geophysical Journal International* **232**(2), 842–863.
- 581 Lavenu, A., T. Winter, and F. Dávila (1995). A Pliocene–Quaternary compressional basin in the Interandean Depression, central Ecuador.  
582 *Geophysical Journal International* **121**(1), 279–300.
- 583 Makropoulos, K. C. and P. W. Burton (1983). Seismic risk of circum-Pacific earthquakes I. Strain energy release. *Pure and Applied*  
584 *Geophysics* **121**, 247–267.
- 585 Marinière, J., J. Nocquet, C. Beauval, J. Champenois, L. Audin, A. Alvarado, S. Baize, and A. Socquet (2020). Geodetic evidence for shallow  
586 creep along the Quito fault, Ecuador. *Geophysical Journal International* **220**(3), 2039–2055.
- 587 McGuire, R. K. (2008). Probabilistic seismic hazard analysis: Early history. *Earthquake Engineering & Structural Dynamics* **37**(3), 329–338.
- 588 McNulty, B. A. (1995). Pseudotachylyte generated in the semi-brittle and brittle regimes, Bench Canyon shear zone, central Sierra Nevada.  
589 *Journal of Structural Geology* **17**(11), 1507–1521.
- 590 Meissner, R. and J. Strehlau (1982). Limits of stresses in continental crusts and their relation to the depth-frequency distribution of shallow  
591 earthquakes. *Tectonics* **1**(1), 73–89.
- 592 Milliner, C., J. Dolan, J. Hollingsworth, S. Leprince, and F. Ayoub (2016). Comparison of coseismic near-field and off-fault surface defor-  
593 mation patterns of the 1992 Mw 7.3 Landers and 1999 Mw 7.1 Hector Mine earthquakes: Implications for controls on the distribution  
594 of surface strain. *Geophysical Research Letters* **43**(19), 10–115.



- 595 Milliner, C. W., J. F. Dolan, J. Hollingsworth, S. Leprince, F. Ayoub, and C. G. Sammis (2015). Quantifying near-field and off-fault  
596 deformation patterns of the 1992 Mw 7.3 Landers earthquake. *Geochemistry, Geophysics, Geosystems* **16**(5), 1577–1598.
- 597 Mora-Páez, H., J. N. Kellogg, J. T. Freymueller, D. Mencin, R. M. Fernandes, H. Diederix, P. LaFemina, L. Cardona-Piedrahita, S. Lizarazo,  
598 J.-R. Peláez-Gaviria, et al. (2019). Crustal deformation in the northern Andes—A new GPS velocity field. *Journal of South American  
599 Earth Sciences* **89**, 76–91.
- 600 Nocquet, J.-M., J. C. Villegas-Lanza, M. Chlieh, P. Mothes, F. Rolandone, P. Jarrin, D. Cisneros, A. Alvarado, L. Audin, F. Bondoux, et al.  
601 (2014). Motion of continental slivers and creeping subduction in the northern Andes. *Nature Geoscience* **7**(4), 287–291.
- 602 Ojo, A. O., H. Kao, Y. Jiang, M. Craymer, and J. Henton (2021). Strain Accumulation and Release Rate in Canada: Implications for Long-  
603 Term Crustal Deformation and Earthquake Hazards. *Journal of Geophysical Research: Solid Earth* **126**(4), e2020JB020529.
- 604 Oskin, M., L. Perg, D. Blumentritt, S. Mukhopadhyay, and A. Iriondo (2007). Slip rate of the Calico fault: Implications for geologic versus  
605 geodetic rate discrepancy in the Eastern California Shear Zone. *Journal of Geophysical Research: Solid Earth* **112**(B3).
- 606 Pagani, M., i. D. Monell, G. Weatherill, L. Danciu, H. Crowley, V. Silva, P. Henshaw, L. Butler, M. Nastasi, L. Panzeri, M. Simionato, and  
607 D. Vigano (2014). OpenQuake engine: An open hazard (and risk) software for the global earthquake model. *Seismological Research  
608 Letters* **85**(3), 692–702.
- 609 Papanikolaou, I. D., G. P. Roberts, and A. M. Michetti (2005). Fault scarps and deformation rates in Lazio–Abruzzo, Central Italy:  
610 Comparison between geological fault slip-rate and GPS data. *Tectonophysics* **408**(1-4), 147–176.
- 611 Parra, H., M. Benito, and J. Gaspar-Escribano (2016). Seismic hazard assessment in continental Ecuador. *Bulletin of Earthquake  
612 Engineering* **14**(8), 2129–2159.
- 613 Reasenber, P. (1985). Second-order moment of central California seismicity, 1969–1982. *Journal of Geophysical Research: Solid  
614 Earth* **90**(B7), 5479–5495.
- 615 Rockwell, T. K., S. Lindvall, T. Dawson, R. Langridge, W. Lettis, and Y. Klinger (2002). Lateral offsets on surveyed cultural features resulting  
616 from the 1999 Izmit and Duzce earthquakes, Turkey. *Bulletin of the Seismological Society of America* **92**(1), 79–94.
- 617 Rodriguez Padilla, A. M., M. A. Quintana, R. M. Prado, B. J. Aguilar, T. A. Shea, M. E. Oskin, and L. Garcia (2022). Near-Field High-  
618 Resolution Maps of the Ridgecrest Earthquakes from Aerial Imagery. *Seismological Research Letters* **93**(1), 494–499.
- 619 Sibson, R. H. (1982). Fault zone models, heat flow, and the depth distribution of earthquakes in the continental crust of the United States.  
620 *Bulletin of the Seismological Society of America* **72**(1), 151–163.
- 621 Stirling, M., T. Goded, K. Berryman, and N. Litchfield (2013). Selection of Earthquake Scaling Relationships for Seismic-Hazard Analysis.  
622 *Bulletin of the Seismological Society of America* **103**(6), 2993–3011.
- 623 Styron, R. (2019). The impact of earthquake cycle variability on neotectonic and paleoseismic slip rate estimates. *Solid Earth* **10**(1), 15–25.
- 624 Tibaldi, A. and L. Ferrari (1992). Latest Pleistocene-Holocene tectonics of the Ecuadorian Andes. *Tectonophysics* **205**(1-3), 109–125.
- 625 Vaca, S., M. Vallée, J.-M. Nocquet, and A. Alvarado (2019). Active deformation in Ecuador enlightened by a new waveform-based catalog  
626 of earthquake focal mechanisms. *Journal of South American Earth Sciences* **93**, 449–461.
- 627 Villegas-Lanza, J. C., M. Chlieh, O. Cavalié, H. Tavera, P. Baby, J. Chire-Chira, and J.-M. Nocquet (2016). Active tectonics of Peru:  
628 Heterogeneous interseismic coupling along the Nazca megathrust, rigid motion of the Peruvian Sliver, and Subandean shortening  
629 accommodation. *Journal of Geophysical Research: Solid Earth* **121**(10), 7371–7394.

- 630 Visage, S., P. Souloumiac, N. Cubas, B. Maillot, S. Antoine, A. Delorme, and Y. Klinger (2023). Evolution of off-fault deformation of  
631 strike-slip fault in a sand-box experiment. *Tectonophysics* **847**, 229704.
- 632 Ward, S. N. (1998). On the consistency of earthquake moment rates, geological fault data, and space geodetic strain: the United States.  
633 *Geophysical Journal International* **134**(1), 172–186.
- 634 Weichert, D. H. (1980). Estimation of the earthquake recurrence parameters for unequal observation periods for different magnitudes.  
635 *Bulletin of the Seismological Society of America* **70**(4), 1337–1346.
- 636 Weldon, R. J. and G. P. Biasi (2013). Appendix I: Probability of detection of ground rupture at paleoseismic sites. *US Geological Survey*  
637 *Open-File Report 2013-1165-I and California Geological Survey Special Report 228-I*.
- 638 Wells, D. L. and K. J. Coppersmith (1994). New empirical relationships among magnitude, rupture length, rupture width, rupture area,  
639 and surface displacement. *Bulletin of the Seismological Society of America* **84**(4), 974–1002.
- 640 Wesnousky, S. G. (2008). Displacement and geometrical characteristics of earthquake surface ruptures: Issues and implications for seismic-  
641 hazard analysis and the process of earthquake rupture. *Bulletin of the Seismological Society of America* **98**(4), 1609–1632.
- 642 Williams, J. N., D. J. Barrell, M. W. Stirling, K. M. Sauer, G. C. Duke, and K. X. Hao (2018). Surface rupture of the Hundalee fault during  
643 the 2016 M<sub>w</sub> 7.8 Kaikōura earthquake. *Bulletin of the Seismological Society of America* **108**(3B), 1540–1555.
- 644 Winter, T., J.-P. Avouac, and A. Lavenu (1993). Late Quaternary kinematics of the Pallatanga strike-slip fault (Central Ecuador) from  
645 topographic measurements of displaced morphological features. *Geophysical Journal International* **115**(3), 905–920.
- 646 Witt, C., J. Bourgois, F. Michaud, M. Ordoñez, N. Jiménez, and M. Sosson (2006). Development of the Gulf of Guayaquil (Ecuador) during  
647 the Quaternary as an effect of the North Andean block tectonic escape. *Tectonics* **25**(3).
- 648 Wu, S.-C., C. A. Cornell, and S. R. Winterstein (1995). A hybrid recurrence model and its implication on seismic hazard results. *Bulletin*  
649 *of the Seismological Society of America* **85**(1), 1–16.
- 650 Yepes, H., L. Audin, A. Alvarado, C. Beauval, J. Aguilar, Y. Font, and F. Cotton (2016). A new view for the geodynamics of Ecuador:  
651 Implication in seismogenic source definition and seismic hazard assessment. *Tectonics* **35**(5), 1249–1279.
- 652 Youngs, R. R. and K. J. Coppersmith (1985). Implications of fault slip rates and earthquake recurrence models to probabilistic seismic  
653 hazard estimates. *Bulletin of the Seismological society of America* **75**(4), 939–964.
- 654 Zinke, R., J. Hollingsworth, and J. F. Dolan (2014). Surface slip and off-fault deformation patterns in the 2013 MW 7.7 Balochistan, Pakistan  
655 earthquake: Implications for controls on the distribution of near-surface coseismic slip. *Geochemistry, Geophysics, Geosystems* **15**(12),  
656 5034–5050.

TABLE 1.

**Hypotheses of probability that a given earthquake occurs on the PPF instead of as background seismicity, as a function of magnitude.**

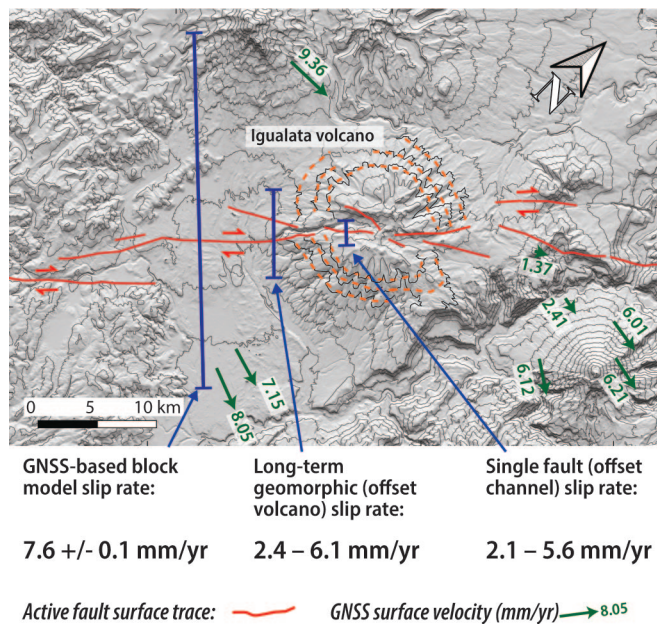
Magnitude	4.9–5.0	5.0–5.5	5.5–6.0	6.0–6.5	6.5–7.0	7.0–7.5	7.5–8.0	8.0
Hypothesis 1	0.1	0.1	0.1	0.4	0.6	0.75	0.95	0.999
Hypothesis 2	0.2	0.4	0.5	0.7	0.7	0.85	0.999	0.999
Hypothesis 3	0.2	0.5	0.6	0.75	0.8	0.9	0.999	0.999

TABLE 2.

**Completeness times for magnitudes**  
modified from [Beauval et al. \(2013\)](#).

Magnitude	4.5–5.0	5.0–5.5	5.5–6.5	6.5–7.0
Year	1963	1957	1920	1860

## Figures



**Figure 1.** Hillshade map of the Pallatanga fault crosscutting the extinct Iguatala volcano with slip rates calculated using three different methods. The geodetic block model considers Global Navigation Satellite System (GNSS) velocities with a large spacing between them ( $> 10$  km) to calculate relative motions between blocks. The long-term geomorphic slip rate uses offset contours of the Iguatala volcano, and considers a fault zone up  $\sim 2 - 5$  km in width. The offset channel slip rate was measured across a single fault strand. 200 m contour spacing. Active fault segments, and geomorphic and offset channel slip rates are from [Baize et al. \(2020\)](#). GNSS velocities and block model slip rate are from [Jarrin \(2021\)](#).

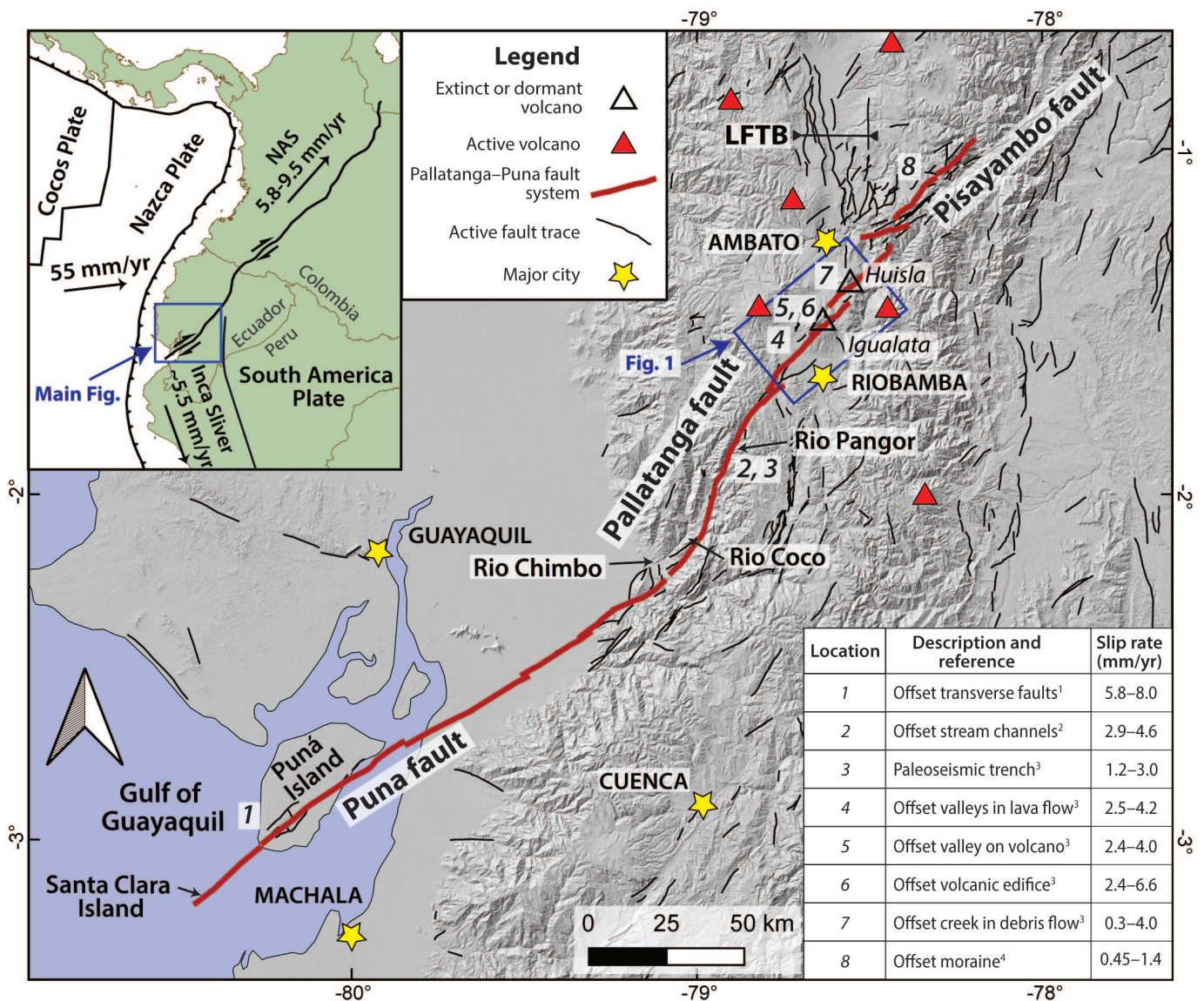


**Figure 2.** Tectonic setting and surface trace of the Pallatanga–Puna fault system (PPF). Inset in top left shows tectonic setting. Northern Andes Sliver (NAS), Inca Sliver, and Nazca Plate motion (with respect to the South America Plate) and boundaries are from [Egbue and Kellogg \(2010\)](#); [Nocquet et al. \(2014\)](#); [Mora-Páez et al. \(2019\)](#); [Jarrin et al. \(2023\)](#). Main figure shows the surface trace of the PPF and right-lateral slip rates. In addition to right-lateral slip on the PPF, the Latacunga fold and thrust belt (LFTB) accommodates east–west crustal shortening, and normal faults in the Gulf of Guayaquil accommodate northwest–southeast extension. Slip rates are listed in the table at bottom right and the locations where they were measured are denoted by numbers. Citations for the slip rates are: 1) [Dumont et al. \(2005\)](#); 2) [Winter et al. \(1993\)](#); 3) [Baize et al. \(2020\)](#); 4) [Champenois et al. \(2017\)](#). PPF surface trace adapted from [Dumont et al. \(2005\)](#); [Champenois et al. \(2017\)](#); [Baize et al. \(2020\)](#) and other active faults are from the [Costa et al. \(2020\)](#) database. Basemap hillshade derived from the Copernicus 30 m DEM.



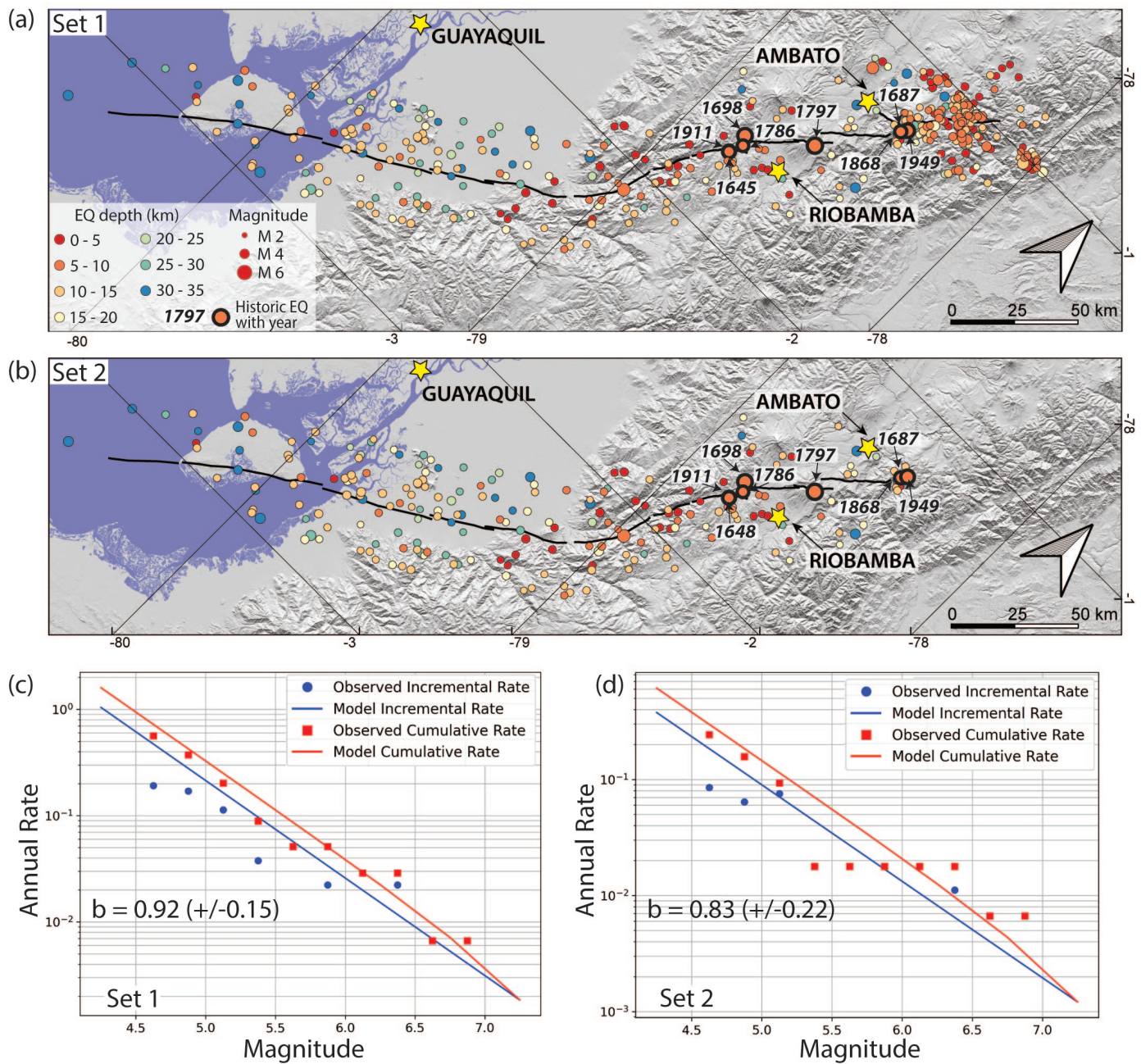


**Figure 3.** Instrumental-historical seismicity associated with the PPF including (a, c) and excluding (b, d) the Pisayambo fault segments. We refer to these fault segment models and catalogues as Set 1 and Set 2 respectively. (a, b) show earthquake epicenters, depths, and magnitudes, and (c, d) show magnitude frequency distributions (MFDs) and  $b$ -values for each catalogue. The completeness table used to calculate  $b$ -values is shown in Table 2. Earthquakes are extracted from a 25 km buffer zone around the fault from the Beauval et al. (2013) catalogue. Basemap hillshade derived from the Copernicus 30 m DEM.

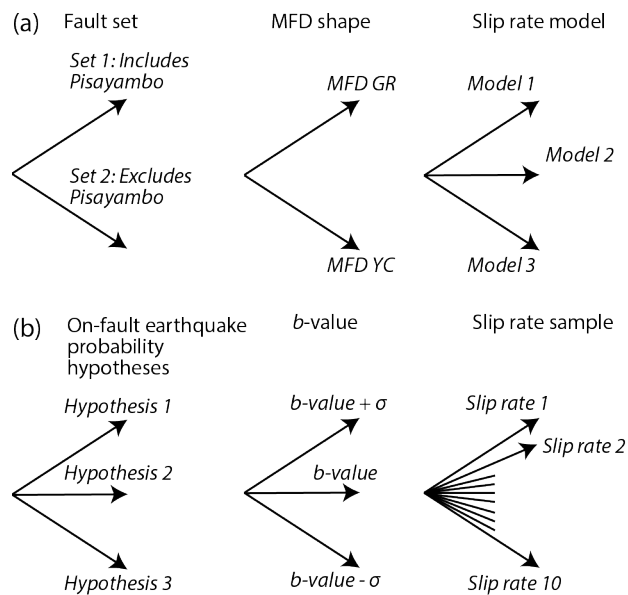


**Figure 4.** Logic tree for the SHERIFS calculations. a) Logic tree branches resulting in 12 independent earthquake rate models based on catalogue and fault segments, MFD shape, and slip-rates. b) Equally weighted logic tree branches within each model run based on on-fault earthquake probability hypotheses, uncertainty in  $b$ -values, and 10 random samples of slip rates from within the range of slip rates designated for each fault segment. The results from these 90 total end branches are plotted together on the same graph to explore uncertainty in each of the independent models described by the branches in (a).

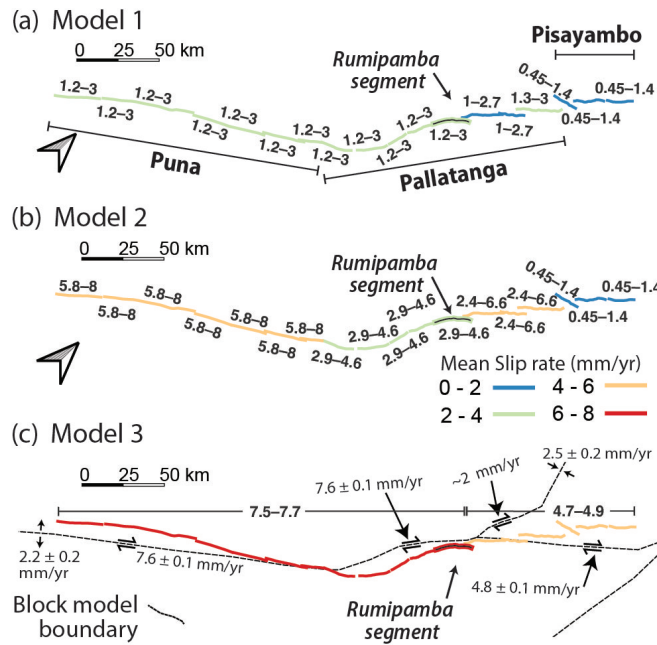


**Figure 5.** Slip rate ranges (in mm/yr) and segments for each of the three slip rate models. Slip rates used in Model 1 (a) and Model 2 (b) are derived from Fig. 2 and those used in Model 3 (c) are derived from geodetic block model boundaries (Jarrin, 2021). The Rumipamba segment has a paleoseismic earthquake rate of one  $M > 7.0$  earthquake every 1000 to 3500 years (Baize et al., 2015), which we compare to the computed participation rates for this fault segment.



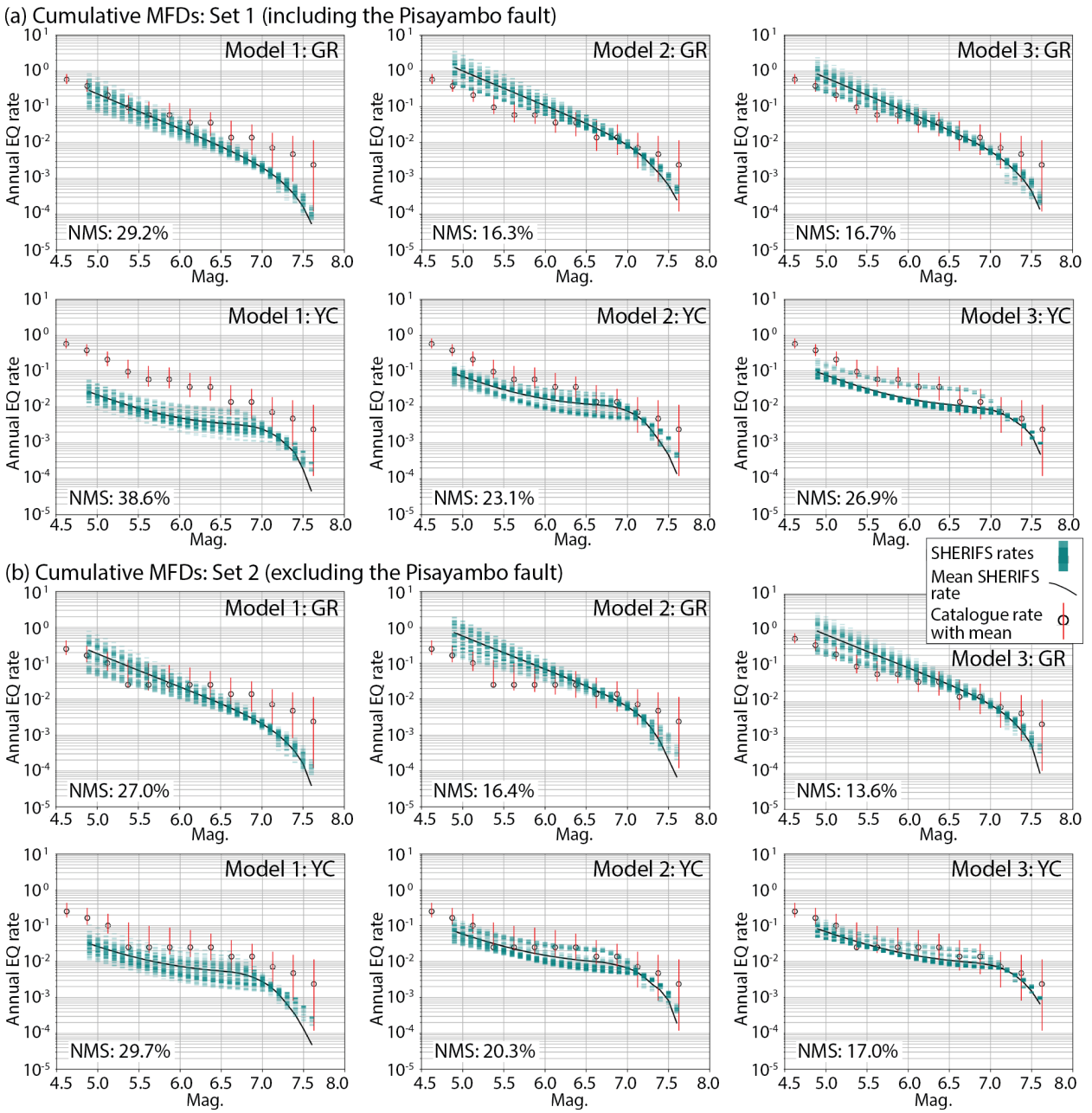


**Figure 6.** Cumulative MFDs computed with SHERIFS for all models with (a) and without (b) the Pisayambo fault segments. Green bars show all results from all branches of the logic tree for each model and the black line is the mean MFD. Black circles show the mean rates in the observed catalogue and red bars show the 95% confidence interval about the mean. All of the computed models use either a Gutenberg-Richter (GR) MFD and hybrid characteristic (Youngs and Coppersmith, 1985) MFD (YC) as predefined MFD shapes to follow. Slip rates for Models 1, 2, and 3 are defined in Fig. 5.

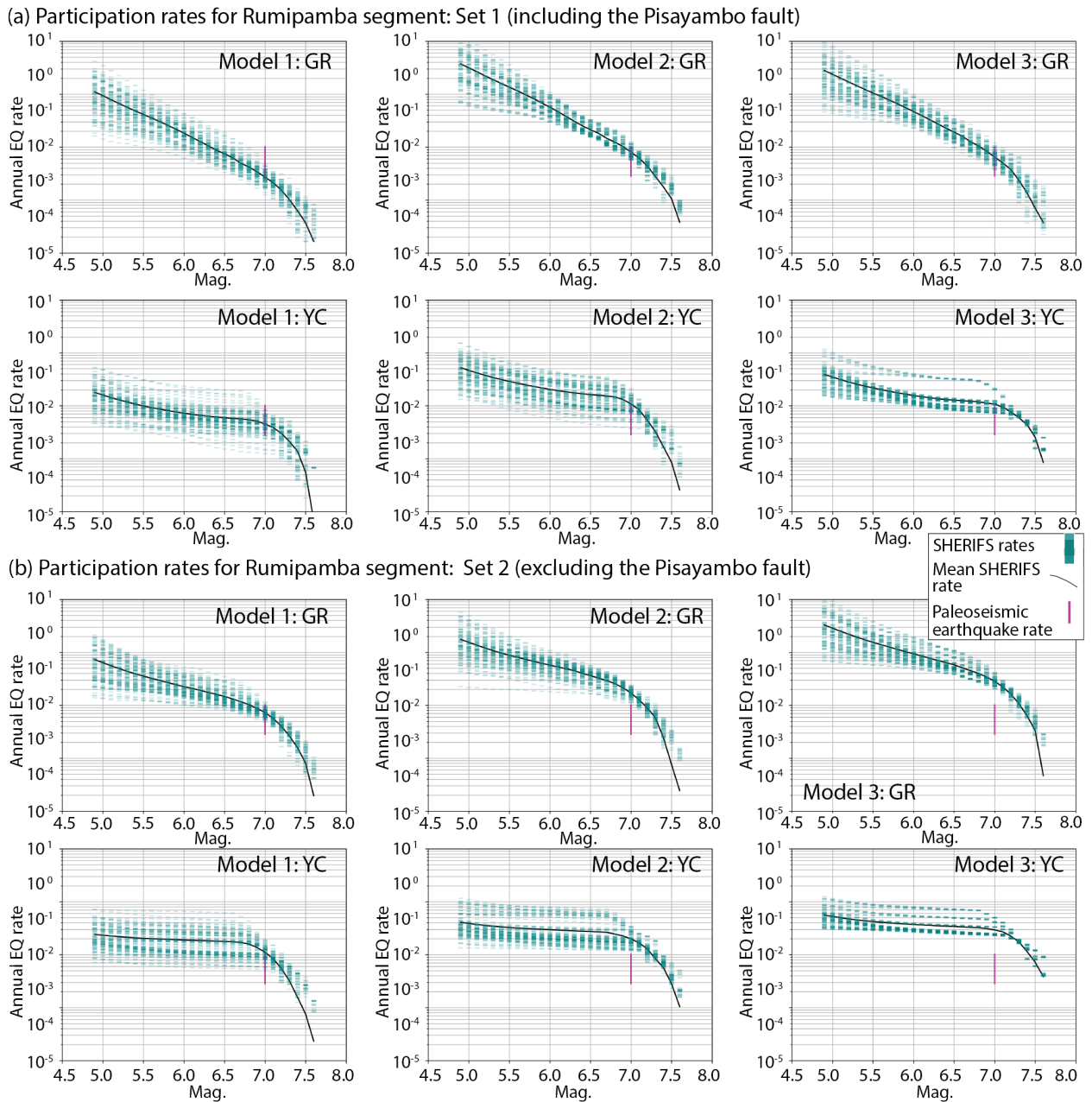


**Figure 7.** Computed cumulative earthquake participation rates for the Rumipamba segment of the PPF compared to paleoseismic earthquake rates from [Baize et al. \(2015\)](#) paleoseismic trench. Set 1 (a) Set 2 (b) use either a Gutenberg-Richter (GR) MFD and hybrid characteristic ([Youngs and Coppersmith, 1985](#)) MFD (YC) as predefined MFD shapes. Slip rates for Models 1, 2, and 3 are defined in Fig. 5. The vertical purple bar indicates the paleoseismic rate of one  $M > 7.0$  earthquake every 1000 to 3500 years.

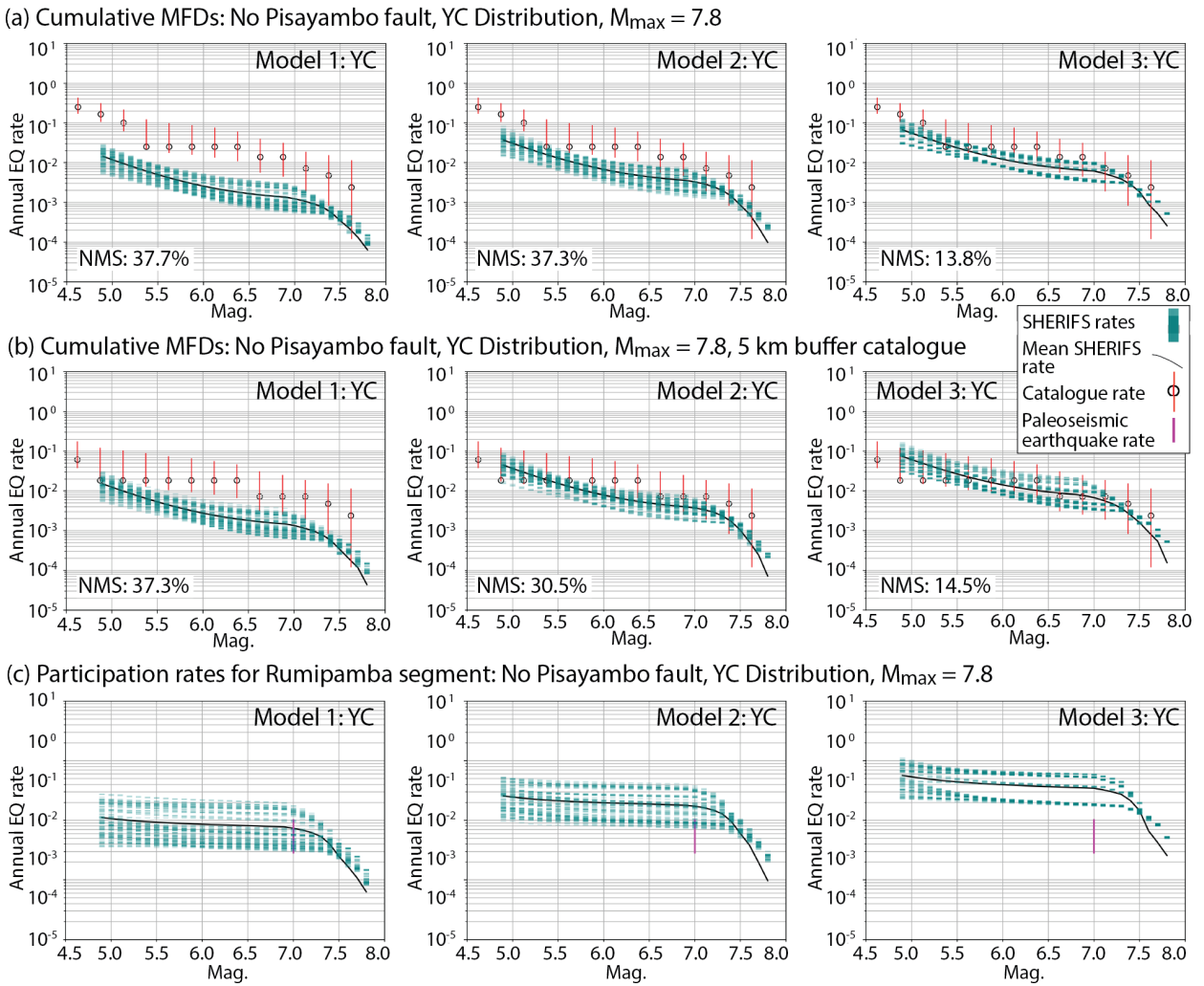


**Figure 8.** SHERIFS computed MFDs considering exclusion of the Pisayambo fault, and an  $M_{\max} = 7.8$  and a hybrid characteristic (YC) MFD as inputs. (a) Computed cumulative MFDs for Models 1-3 compared with the original catalogue or (b) a 5 km buffer zone catalogue. (c) Computed cumulative earthquake participation rates for the Rumipamba segment of the PPF compared to paleoseismic earthquake rates from the [Baize et al. \(2015\)](#) paleoseismic trench. Slip rates for Models 1, 2, and 3 are defined in Fig. 5.